Microstructure refinement, mechanical and biocorrosion properties of Mg–Zn–Ca–Mn alloy improved by a new severe plastic deformation process

M. Kavyani [a], G.R. Ebrahimi [a,*], H.R. Ezatpour [b], M. Jahazi [c]

[a] *Materials and Metallurgical Engineering Department, Faculty of Engineering, Ferdowsi University of Mashhad, Mashhad 9177948974, Iran*
[b] *Faculty of Engineering, Sabzevar University of New Technology, Sabzevar, Iran*
[c] *Department of Mechanical Engineering, École de Technologie Supérieure, Montréal, PQ, Canada*

Abstract

In this study, the microstructural evolution, mechanical properties and biocorrosion performance of a Mg–Zn–Ca–Mn alloy were investigated under different conditions of heat treatment, extrusion, one pass and two passes of half equal channel angular pressing (HECAP) process. The results showed significant grain refinement of the homogenized alloy after two passes of HECAP process from $345\,\mu m$ to $2\,\mu m$. Field emission scanning electron microscopy (FESEM) revealed the presence of finer $Mg_6Zn_3Ca_2$ phase as well as α-Mn phase after HECAP process. The results also showed that mechanical characteristics such as yield strength, ultimate tensile strength and elongation of the HECAPed samples improved by $\sim$208%, $\sim$144% and $\sim$100% compared to the homogenized one, respectively. Crystallographic texture analysis indicated that most of the grains at the surface were reoriented parallel to the (0001) basal plane after HECAP process. Electrochemical corrosion tests and immersion results indicated that the sample with two passes of HEACP had the highest biocorrosion resistance confirming that the basal planes had the lowest corrosion rate compared to the non-basal ones. The mechanical behavior and bio-corrosion evaluation demonstrated that the HECAPed Mg–Zn–Ca–Mn alloy has great potential for biomedical applications and a mechanism was proposed to explain the interrelations between the thermomechanical processing and bio-corrosion behavior.
© 2020 Published by Elsevier B.V. on behalf of Chongqing University.
This is an open access article under the CC BY-NC-ND license (http://creativecommons.org/licenses/by-nc-nd/4.0/)
Peer review under responsibility of Chongqing University

1. Introduction

Thanks to the low density of magnesium and suitable mechanical characteristics, such as moderate ductility (fracture strain $\geq$ 15%) and relatively high specific strength (UTS $\geq$ 250 MPa), elastic modulus close to that of the human bone, the development of magnesium and its alloys in orthopedic and cardiovascular applications as well as scaffolds for tissue engineering has been continuously increased in recent years [1–3]. However, the widespread application of these alloys requires further improvement in their mechanical properties

and better corrosion resistance as magnesium and its alloys are remarkably susceptible to corrosion damage in media such as human body fluid [4,5].

The addition of alloying elements is one of the approaches used in order to enhance the mechanical and corrosion properties of magnesium alloys. Among all studied alloy systems, Mg–xZn–xCa based series have been reported to have great potential as biodegradable implants, because Mg, Zn and Ca are essential nutritional elements with no deleterious side effects (such as Alzheimer or allergic disease) for human health [6–8]. Cho et al. [9] found that the addition of Mn to Mg–4Zn–0.5Ca alloy is beneficial for decreasing the corrosion rate due to the formation of a dense layer of MnO and MnO_2 on the surface of the alloy which protects the Mg

* Corresponding author.
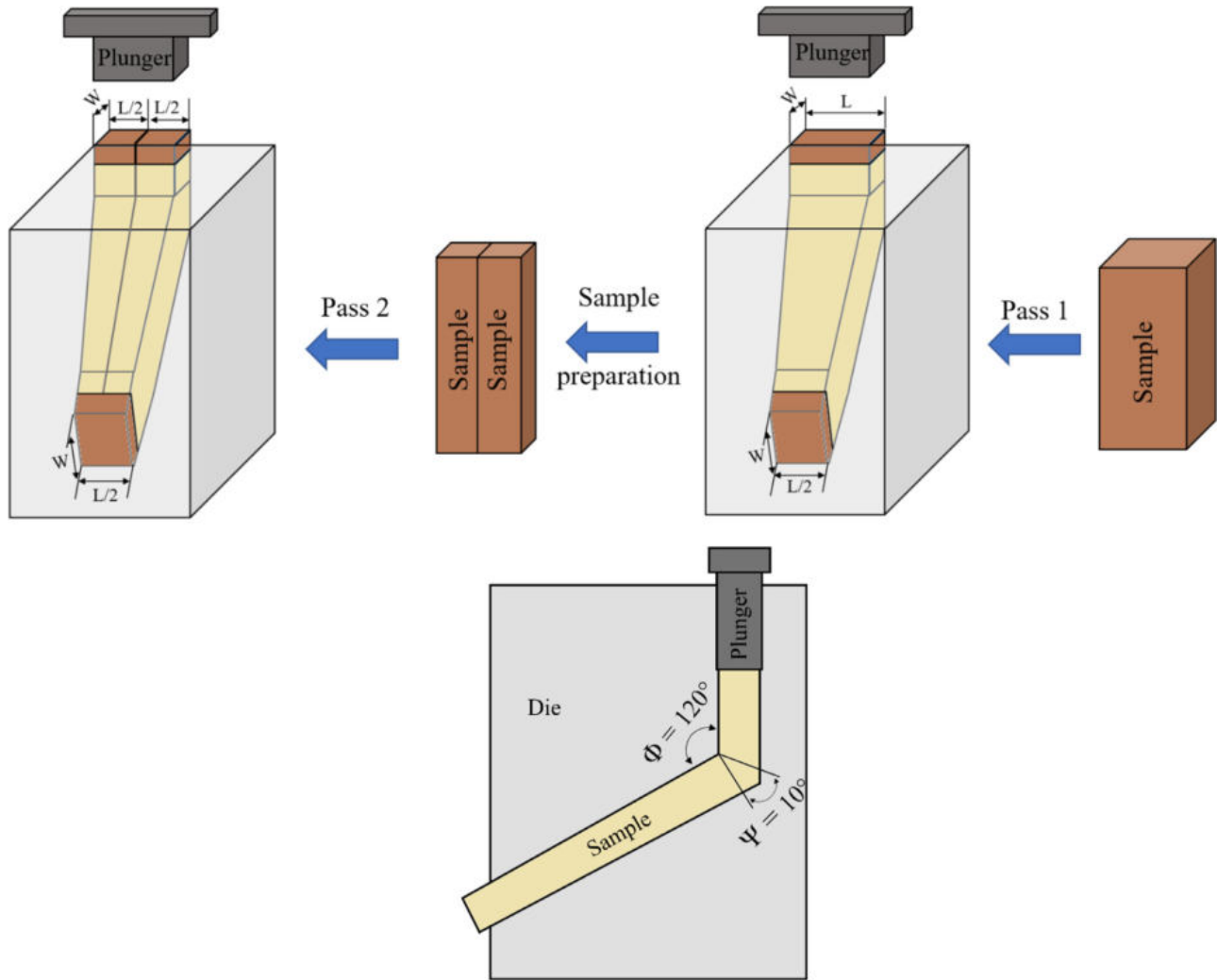*E-mail address:* r.ebrahimi@um.ac.ir (G.R. Ebrahimi).

Fig. 1. Schematic setup of HECAP process.

matrix from chloride penetration. However, cast bio-Mg alloys such as Mg–Ca [10], Mg–Zn [11], Mg–Zn–Ca [12] and Mg–Zn–Ca–Mn [13] alloys have limited use as biodegradable implants because of their poor mechanical properties. The strength of a Mg–Zn alloy reduced rapidly after an immersion time of 72 h from 625 MPa to 390 MPa [14]. Li and coworkers [15] reported that the mechanical properties (strength and ductility) of a commercial Mg–Ca alloy are not adequate for load-bearing applications and the corrosion resistance was not sufficient. In another study, Zhang et al. [16] examined the mechanical properties of a Mg–Zn–Ca alloy and a Mg–Zn–Ca–Mn alloy. They found that maximum tensile strength values of 185 MPa and 390 MPa are not acceptable for biomedical applications and corrosion resistance is another important factor. Therefore, it appears that the addition of alloying elements cannot remarkably improve both mechanical and corrosion resistances and thermal and/or thermomechanical treatments need to be considered.

Ultrafine-grained (UFG) materials and their other enhanced properties have mostly attracted interests due to their high strength. Severe plastic deformation (SPD) processing [17] is one of the most successful approaches for production of grain refinement materials with the new small grains and high angle grain boundaries (HAGBs). However, an ultra-high effective strain is necessary to achieve such submicron grains with HAGBs while the conventional deformation processes such as rolling, extrusion, and drawing with medium or high strains cannot meet this expectation. Equal channel angular pressing (ECAP) [18], high pressure torsion (HPT) [19], torsional-equal channel angular pressing (T-ECAP) [20], and cone–cone method (CCM) [21], as well as introducing novel SPD techniques such as twist extrusion (TE) [22], planar twist extrusion (PTE) [23], simple shear extrusion (SSE) [24], planar twist channel angular extrusion (PTCAE) [25], tube channel pressing (TCP) [26] and cyclic extrusion compression (CEC) [27] have commonly developed as effective SPD methods for production of UFG materials. Generally, in SPD techniques, like ECAP the first and second passes are the key on the final microstructure and properties due to higher grain refining rate [18]. Generally, in SPD techniques, the geometrical dimensions and the shape of the processed sample remain unchanged while leads to apply the lower effective plastic strain
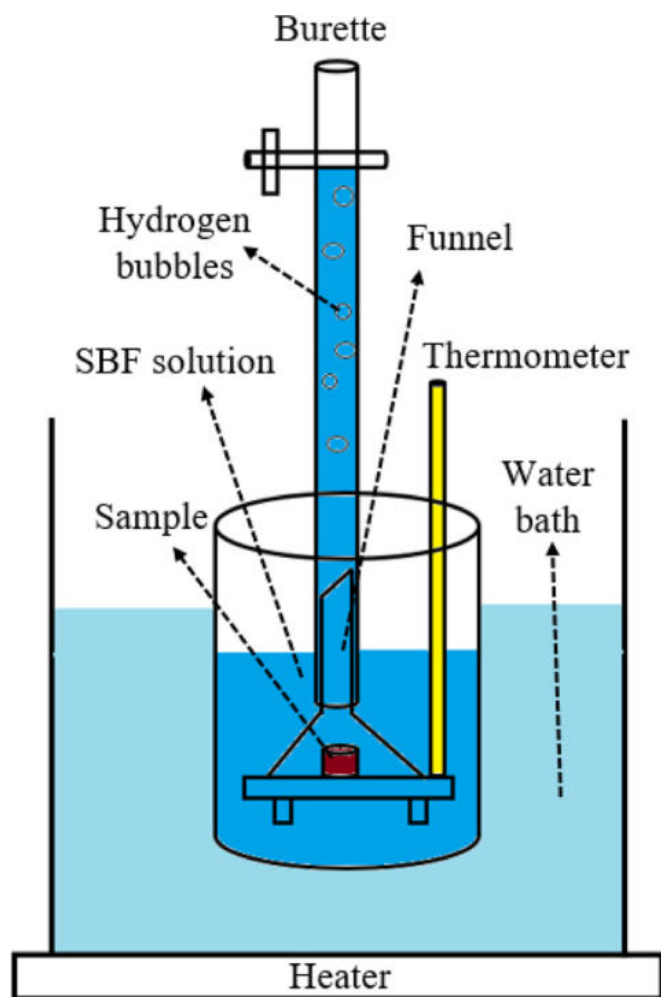
Fig. 2. Schematic setup for hydrogen evolution test.

during process. Recently, researchers applied SPD techniques combined with direct extrusion process such as torsion extrusion (TE) [28], forward shear normal extrusion (FSNE) [29] and present work while the extrusion provided a great potential in grain refining after the first pass of treatment.

Researches have reported that thermomechanical processes such as extrusion [30-32] as well as severe plastic deformation [33-34] can noticeably refine the microstructure of Mg alloys and improve their mechanical properties and bio-corrosion resistance. Specifically, Gao et al. [30] reported that the application of high pressure torsion (HPT) leads to uniform corrosion of Mg–Zn–Ca alloy due to a more homogenous distribution of second phase particles. Peng et al. [35] showed that after cyclic extrusion compression (CEC) treatment of a Mg–10Gd–2Y–0.5Zr alloy at 450 °C, the yield strength (YS) increases from 225 MPa to 247 MPa and ductility from 6% to 22%. Wu et al. [36] also reported that YS, ultimate tensile strength (UTS) and elongation, of a Mg–Zn–Y–Nd alloy processed by CEC increase by about 20%, compared to the as-cast one. Interestingly, their results showed that the CEC treatment results in a decrease of the corrosion current density from 2.8×10^{-4} A/cm^2 to 6.6×10^{-5} A/cm^2. Birbilis et al.

[37] reported that the application of equal channel angular pressing (ECAP) reduces both anodic and cathodic reaction kinetics in pure magnesium and found that the ECAP-ed material, characterized by a finer grain size, has a lower corrosion current density and hence lower corrosion rate. Furthermore, Zhang et al. [34] investigated the effect of HPT and annealing treatment on corrosion resistance of a Mg–Zn–Ca alloy. The HPT process was performed at room temperature for up to five revolutions and subsequent annealing at 90–270 °C for 30 min. The results showed that with the increment of annealing temperature, the grain size of HPT alloy is significantly refined. The results also indicated that the best corrosion resistance is achieved at 210 °C due to the increase in the number of (0002) oriented grains and the decrease in surface stresses.

Another major factor that has great impact on mechanical and corrosion properties is the distribution of second phase particles. Zhang et al. [38] studied Mg–Zn–Ca–Mn alloys, and reported that when the atomic ratio of Zn/Ca is less than 1.2, Mg_2Ca and $Mg_6Zn_3Ca_2$ precipitates form while when the atomic ratio is more than 1.2 only $Mg_6Zn_3Ca_2$ forms. The formation of Mg_2Ca phase results in a remarkable decrease in strength and ductility and an improvement in the corrosion resistance. In another work [39], the same authors investigated the effect of cerium addition on biocorrosion resistance of Mg–2Zn–0.5Mn–Ca alloy. They found that the distribution of $Mg_6Zn_3Ca_{2 s}$ phase changes through the formation of Mg_2Ca and $Mg_{12}CeZn$ particles. The uniform distribution of a large fraction of particles throughout the microstructure causes the formation of a dense and tenacious protective film layer and enhances the biocorrosion resistance. The formation of fine precipitates can also have an additional effect in increasing the corrosion resistance. For example, Bakhsheshi-Rad et al. [40] reported that the addition of Mn and Zn to a Mg–Ca alloy results in significant precipitation and grain refinement which ultimately enhances the corrosion resistance of the alloy.

A common finding in all above mentioned studies is that a fine grain microstructure plays a crucial role in improvement of the mechanical properties and produces residual compressive stresses in the Mg substrate which ultimately enhances the corrosion resistance. The effect of alloying elements and particularly Mg_2Ca in improving the mechanical and corrosion properties of cast Mg–Zn-based alloys was also clearly revealed. However, little information is available on the effect of thermomechanical processing (TMP), and particularly severe plastic deformation (SPD), on microstructural evolution and bio-corrosion behavior of Mg–Zn–Ca–Mn alloys. Specifically, the role of second phase particles and particularly $Mg_6Zn_3Ca_{2 s}$ phase, which can dynamically precipitate during deformation on mechanical and bio-corrosion behavior is not clear. Furthermore, the influence of TMP or SPD on the evolution of crystallographic texture, as a critical element in microstructure evolution has not been clarified yet.

In the present study a new SPD treatment, HECAP, composed of combination of ECAP and extrusion is used to study the effect of high temperature deformation conditions on microstructure and texture evolution of a Mg–Zn–Ca–Mn alloy
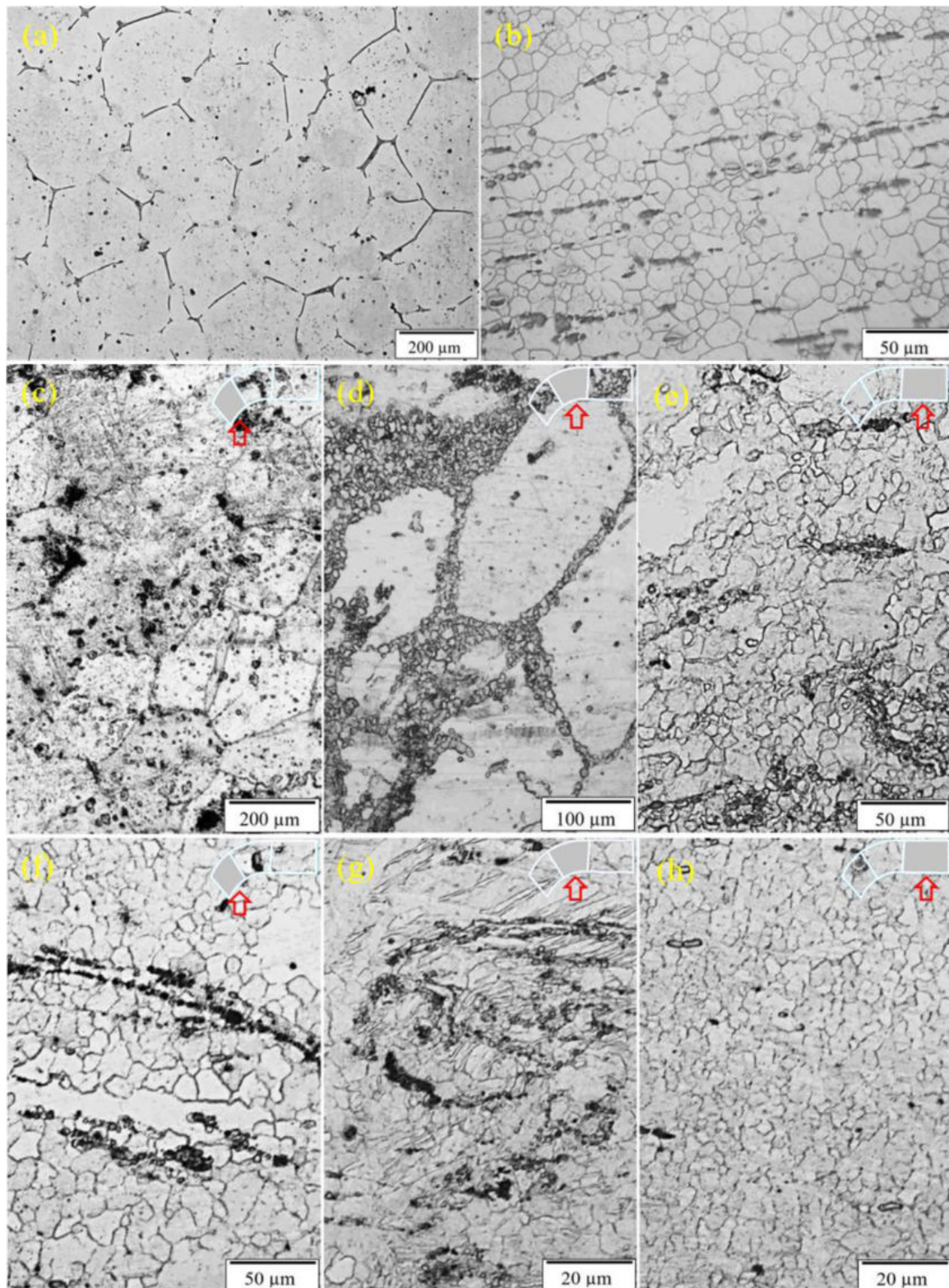
Fig. 3. Optical microstructure of Mg–Zn–Ca–Mn alloy at different conditions; (a) homogenized, (b) extrusion, three different region of one-pass HECAP, (c) homogenized, (d) ECAP, (e) extrusion, three different region of two-HECAP; (f) homogenized, (g) ECAP, (h) extrusion and (i) EDS result of second phase.

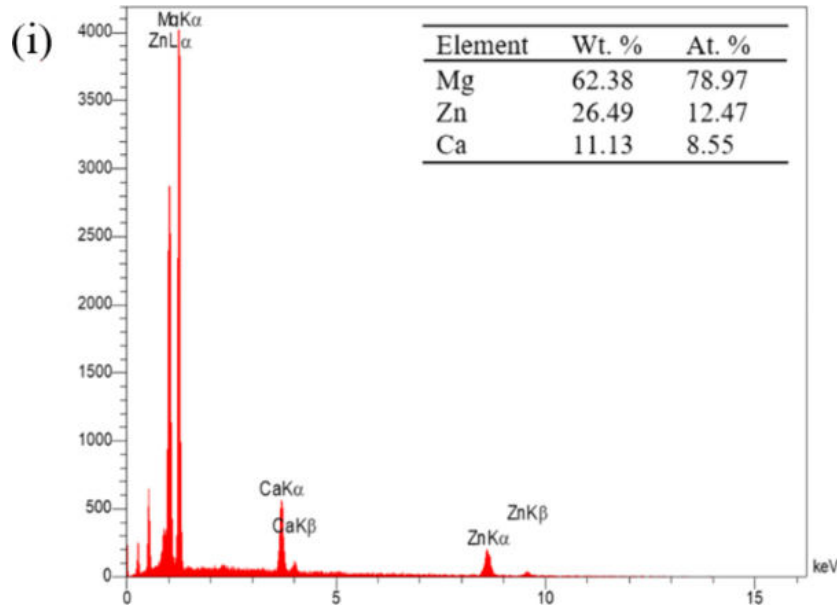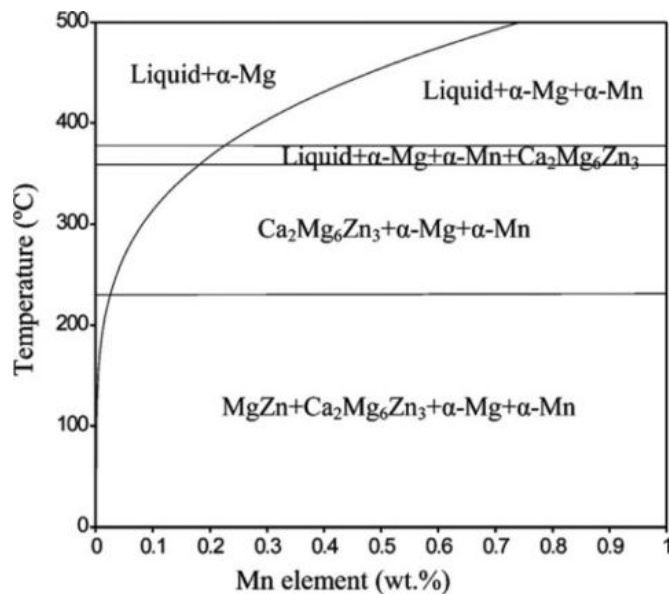| Element	Wt. %	At. %
Mg	62.38	78.97
Zn	26.49	12.47
Ca	11.13	8.55

Fig. 3. Continued

Fig. 4. The phase diagram of Mg–Zn–Ca–Mn alloy [46].

with particular focus on the role of second phase particles on mechanical and bio-corrosion performance.

2. Experimental materials and methods

2.1. Material preparation

The Mg–Zn–Ca–Mn alloy was fabricated by stir casting using high purity Mg (99.99%), Zn (99.99%), Ca (99.99%) and Mn (99.99%) as raw materials. Mg, Zn, Ca and Mn were charged into a stainless-steel crucible placed in an electrical resistance furnace. The melting process was performed at 800 °C for 2h with mechanical stirring under argon at-

Table 1
Chemical composition of Mg–Zn–Ca–Mn alloy (in wt%).

Alloy	Zn	Ca	Mn	Mg
Mg–Zn–Ca–Mn	3.95	0.5	0.75	Bal

mosphere to inhibit oxidation and minimize evaporation of alloying elements. Then, the melt was stirred for 20 min to dissolve and uniformly disperse the alloying elements. After the stirring treatment, the melt was poured into a preheated mold at 450 °C. The chemical composition of the Mg–Zn–Ca–Mn alloy measured by inductively coupled-plasma atomic emission spectrometry (ICP-AES) is provided in Table 1.

The twelve cast ingots were homogenized at 420 °C for 24 h in an electric furnace with a temperature accuracy of ± 5 °C and finally quenched in water. Some of the homogenized samples were extruded into cylindrical rods with an extrusion ratio of 4:1 at 300 °C and extrusion speed of 2 mm/min. Other samples were HECAPed two passes at 300 °C using a ram speed of 2 mm/min and a ratio of 2:1. The schematic setup of the HECAP process is shown in Fig. 1. During the extrusion and HECAP processes the die and the samples were lubricated with graphite to reduce the interfacial friction.

2.2. Mechanical properties and microstructure characterization

The tensile and compression samples were prepared according to the ASTM E8-04 [41] and E9-09 [42] ASTM standards, respectively. All tensile and compression samples were machined from the extruded bars and HECAPed billets along the extrusion (longitudinal) direction. The tensile and compression tests were carried out at room temperature at
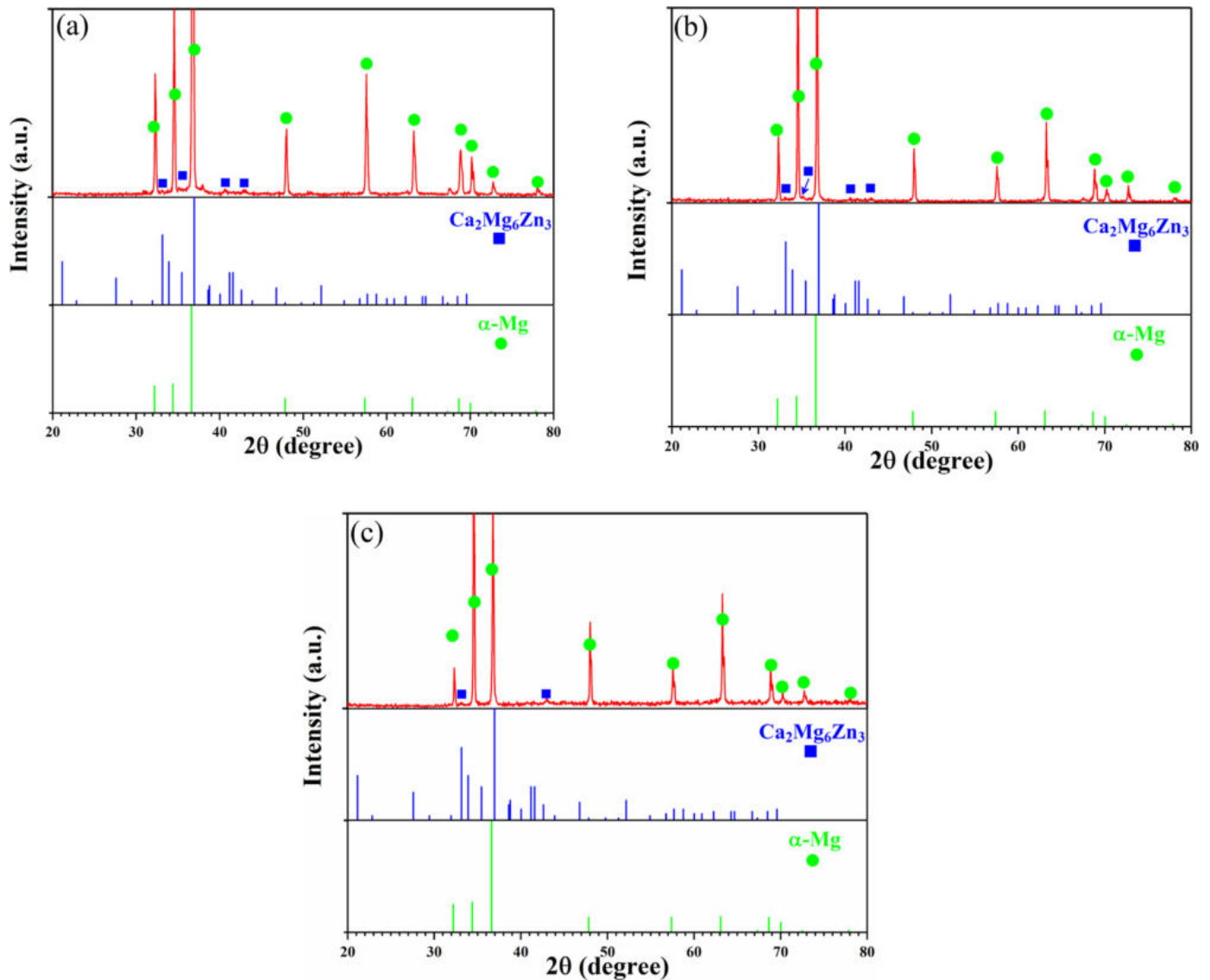
Fig. 5. XRD patterns of Mg–Zn–Ca–Mn alloy at different conditions of (a) homogenization, (b) one-pass HECAP and (c) two-pass HECAP.

a strain rate of $1 \times 10^{-3}\,s^{-1}$ using a zwick-roell Z250 testing machine. The fracture surfaces of the tensile specimens were characterized by a MIRA 3 TESCAN field emission scanning electron microscope (FESEM).

For metallographic examination, samples were ground with SiC emery papers up to 5000 grit, mechanically polished and ultrasonically cleaned with distilled water between each polishing step. They were then etched with 5 ml acetic acid, 6 g picric acid, 10 ml distilled water and 100 ml ethanol and examined by optical microscopy (OM) and the FESEM in backscatter electron mode for observation of corrosion morphology and energy-dispersive spectrometry (EDS) for identification of second phases and corrosion products. Moreover, a Bruker D8 advanced X-ray diffractometer with a Cu Kα radiation source was used to evaluate the phases and the macrotexture of the samples. The grain size measurement was carried out using linear intercept method according to the ASTM standard E112-G6.

2.3. Electrochemical test

Electrochemical tests were performed using standard equipment (IviumStat model) to investigate the corrosion performance of the alloy under different conditions in the simulated body fluid (SBF) [40] solution at 37 °C. For this purpose, the cylindrical samples were connected with copper wire and mounted in an epoxy resin in which the exposed area of all specimens was 0.785 cm^2. A three-electrode cell was employed with Ag/AgCl reference electrode, platinum as the counter electrode and the sample as the working electrode. The open circuit potential was measured for 1200s to establish steady state prior to the start of the potentiodynamic polarization (PDP) test. All PDP tests were conducted at a constant scan rate of 0.5 mV/s in the potential range of −0.250 mV to 250 mV. The electrochemical impedance spectroscopy (EIS) technique was used in the frequency range of 100 kHz–10 mHz with an amplitude of 20 mV for all samples.

Table 2
The composition of 1000 ml Kokubo's SBF (pH 7.4).

Order	Reagent	Amount (g/L)
1	NaCl	7.996
2	NaHCO$_3$	0.350
3	KCl	0.224
4	K$_2$PO$_4$. 3H$_2$O	0.228
5	MgCl$_2$. 6H$_2$O	0.305
6	1 M - HCl	40 ml
7	CaCl$_2$	0.278
8	Na$_2$SO$_4$	0.071
9	(CH$_2$OH)$_3$ CNH$_2$	6.057

2.4. Immersion test

In order to evaluate the bio-corrosion behavior of the investigated alloy under different conditions, hydrogen evolution tests were conducted using the SBF solution at 37±0.5 °C according to the ASTM G31-72 standard [43]. The setup for hydrogen evolution test is schematically shown in Fig. 2 and the composition of the SBF solution is presented in Table 2. Before the immersion of the samples in the SBF solution, all samples were embedded in an epoxy resin so that the ratio of the sample surface to the SBF volume was 1 cm^2. The surface of the sample was then polished to reach mirror like state and immersed in the SBF solution (25 ml) in sterilized bottle surrounded by water bath at 37 °C for 7 days. After that, the samples were removed and rinsed with distilled water and dried at room temperature. In this study, the hydrogen evolution rate was calculated in ml cm^{-2} day^{-1}.

3. Results and discussions

3.1. Microstructure characterization

The optical microstructure of the homogenized, extruded and HECAPed samples along with the chemical composition of the second phase particles characterized by EDS are shown in Fig. 3. In general, the microstructure consists of α-Mg matrix alongside second phase particles distributed at the grain boundaries and grain interiors. The average grain size of homogenized and extruded samples is 347.26 μm (Fig. 3(a)), 16.46 μm (Fig. 3(b)) and the average grain size of HECAP at different sections namely homogenized, ECAP-ed and extruded for first pass is 333.34 μm (Fig. 3(c)), 35.46 μm (Fig. 3(d)), 14.64 μm (Fig. 3(e)) and for second pass is 12.84 μm (Fig. 3(f)), 7.6 μm (Fig. 3(g)) and 2.24 μm (Fig. 3(h)), respectively. The results clearly reveal that the HECAP process has a remarkable grain refining effect on the alloy microstructure with the presence of uniform equiaxed grains throughout the microstructure (Fig. 3(c–h)). The microstructure of the extruded and one-pass HECAPed samples has been characterized with the presence of coarse grains surrounded by fine recrystallized grains indicating incomplete recrystallization. As can be seen in Fig. 3(d–f),

some coarse grains surrounded by pretty fine grains can be representative of dynamic recrystallization (DRX) or necklace microstructure, in which new small grains are located along larger deformed grain boundaries. In other words, the new dislocation-free grains nucleate at prior deformed grain boundaries. After two passes of HECAP, the alloy microstructure becomes more homogenous and finer (Fig. 3(h)) due to extensive dynamic recrystallization. It must be also noted that some precipitation particles are visible along the grain boundaries and grains interior. Some of the grain boundary second phase particles have a gird like shape. It appears that the high pressure induced by the HECAP process leads to the fragmentation of the grains as well as the second phase particles resulting in a refined and more homogenous microstructure, as also reported by Wu et al. [36].

As shown in Fig. 3(a), the coarse grain structure of the homogenized sample is probably due to the occurrence of a grain coalescence process taking place after dissolution of the second phase precipitates [44]. After one pass of HECAP, a bimodal grain size distribution can be observed with some grains with an average size of about 34.2 μm and others about 14.2 μm. But after two passes, the large grains disappear and more homogenous and uniform grain size is obtained, as shown in Fig. 3(c–h). It is well-known that the nucleation of new DRXed grains is proportional to the stored plastic strain energy. Since the stored plastic energy is not uniform, then the recrystallization rate is expected to vary over different regions of the microstructure [45]. Hence, both coarse and fine grains could be the result of DRX. However, the microstructure of the two-pass HECAPed sample is more homogenous and consists of fine grains with an average grain size of about 2 μm.

The composition of the particles was characterized by EDS, as shown in Fig. 3(i). The mole ratio of n(Mg):n(Zn):n(Ca) in the second phase is about 6:3:2 which reveals the chemical formula of this phase is Mg$_6$Zn$_3$Ca$_2$. This finding confirms that the Mg$_2$Ca intermetallic phase has not been formed in the microstructure and the lamellar eutectic phase is only composed of α-Mg and Mg$_6$Zn$_3$Ca$_2$ at the grain boundaries, as also reported by other authors [45]. However, the phase diagram of Mg–Zn–Ca–Mn alloy calculated by Pandat software is observed in Fig. 4 [46]. Fig. 4 illustrates the formation of every single phase of Mg–Zn–Ca–Mn and represents that what phase is thermodynamically formed and stabled at various temperatures. It shows that the microstructure consists of α-Mg+Mg$_6$Zn$_3$Ca$_2$+α-Mn at ∼ 230–360 °C. In other words, α-Mn phase in this alloy can be formed at temperatures below ∼ 360 °C, but it is difficult to observe by optical microscope due to its trace addition.

The evolution of the volume fraction of second phase particles is an important microstructural feature that must be taken into consideration. Specifically, the volume fraction of the particles is significantly reduced after HECAP process compared to the undeformed sample, as can be seen in Fig. 3. XRD results illustrated in Fig. 5 also indicate the decrease of Mg$_6$Zn$_3$Ca$_2$ phase after HECAP process. It
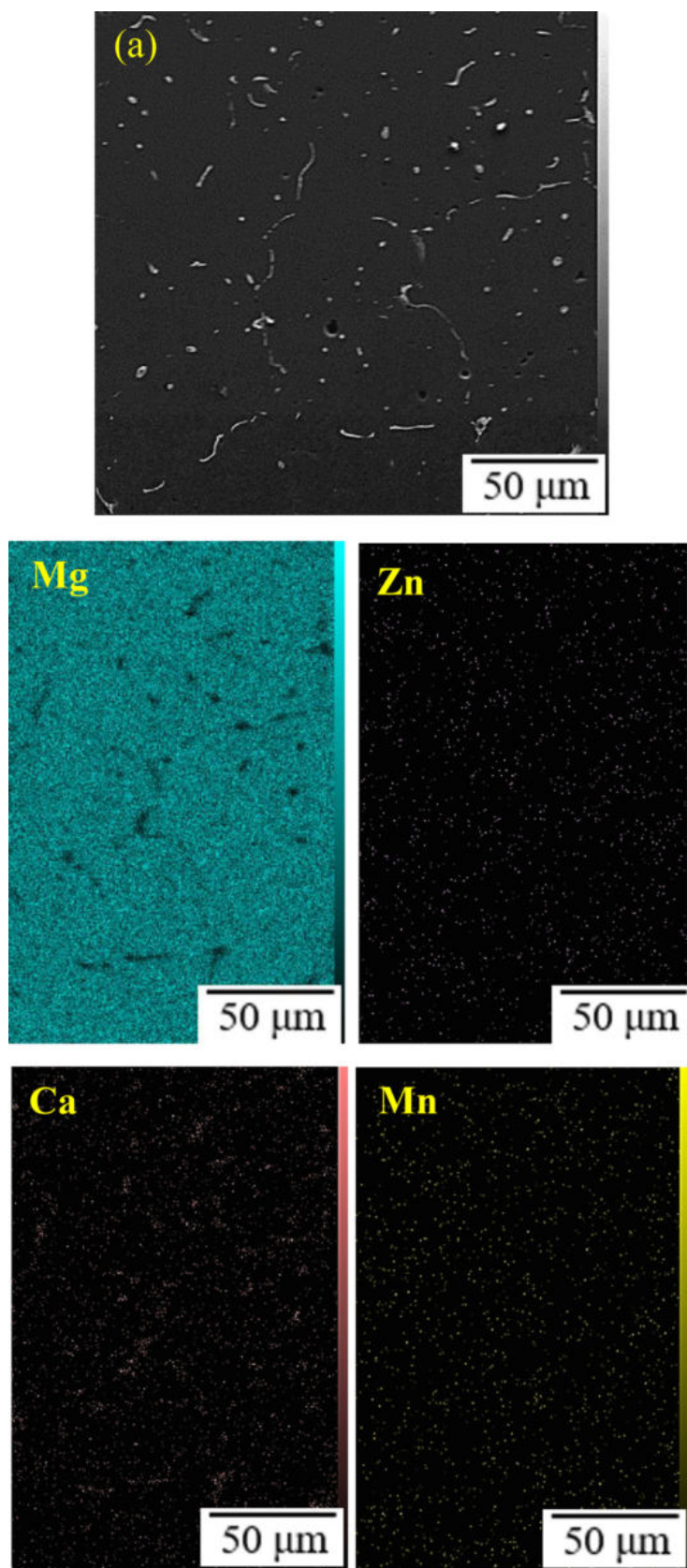
Fig. 6. (a) EDS elemental map of homogenized sample, FESEM images of second phase particles of at different conditions of (b) homogenizion, (c) extrusion, (d) one-pass HECAP, (e) two-pass HECAP, (f) EDS analysis of $Mg_6Zn_3Ca_2$ and (g) EDS analysis of α-Mn.
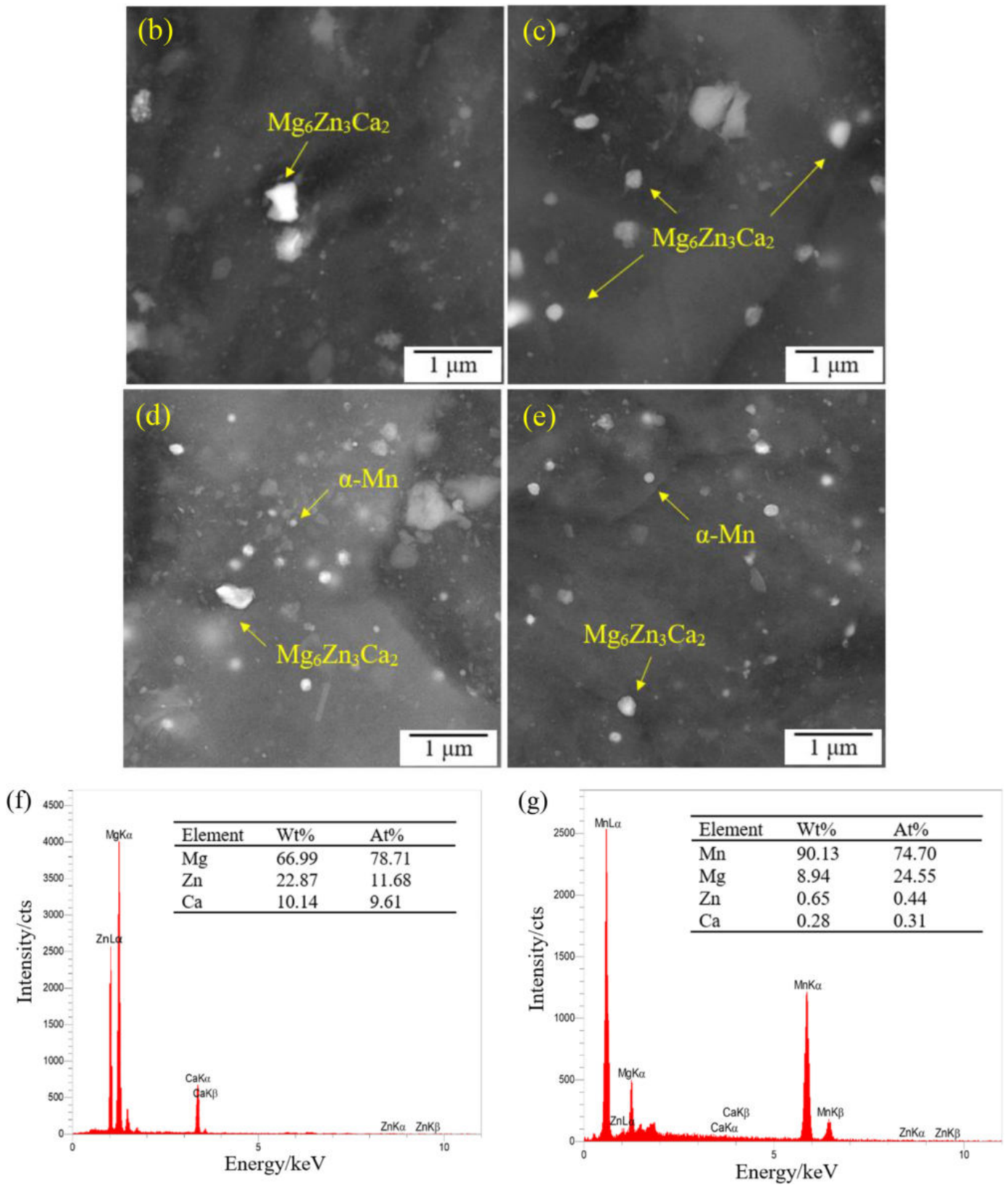
Fig. 6. Continued

ARTICLE IN PRESS

JID: JMAA [m5+;December 19, 2020;18:54]

M. Kavyani, G.R. Ebrahimi, H.R. Ezatpour et al.   Journal of Magnesium and Alloys xxx (xxxx) xxx

(f)

Element	Wt%	At%
Mg	66.99	78.71
Zn	22.87	11.68
Ca	10.14	9.61

(g)

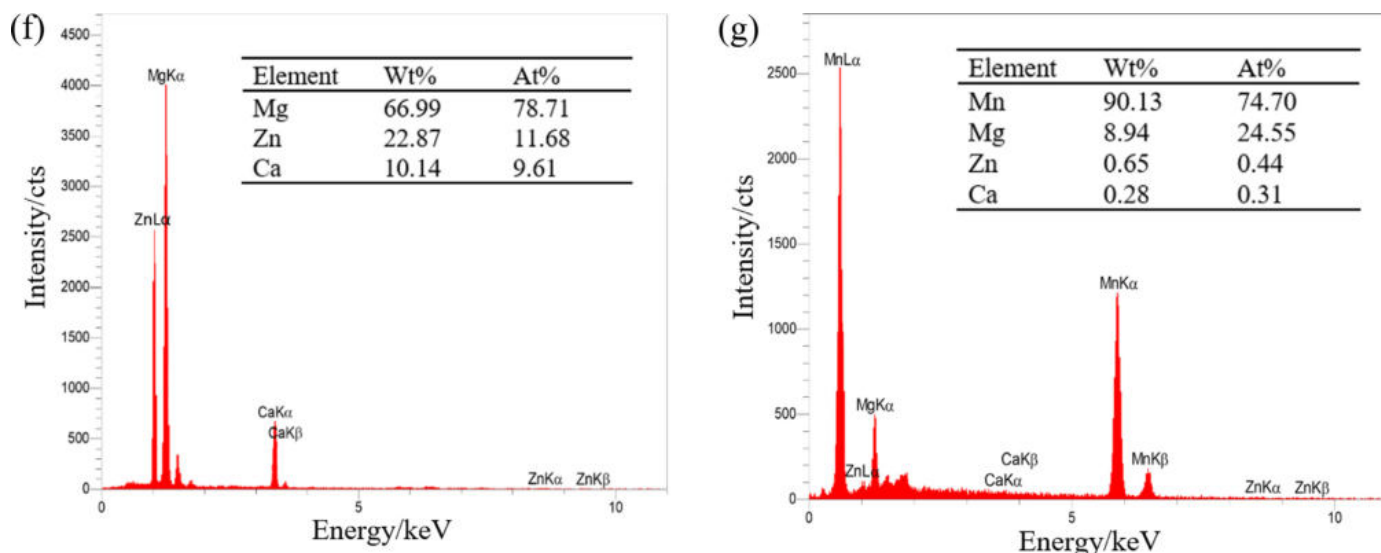| Element	Wt%	At%
Mn	90.13	74.70
Mg	8.94	24.55
Zn	0.65	0.44
Ca	0.28	0.31

Fig. 6. Continued

should be mentioned that α-Mn phase peak was not observed by XRD analysis due to its trace addition. The decrease of $Mg_6Zn_3Ca_2$ phase could be attributed to the dissolution of the grain boundary particles into the α-Mg matrix during the SPD process. The dissolution is accelerated due to the high density of defects (dislocations and vacancies), generated as a result of thermomechanical processing, which provide high diffusion paths for Zn and Ca atoms [45]. Moreover, the high pressure induced by the HECAP treatment can possibly lead to the fragmentation of second phase particles which could not be seen by optical microscopy as also reported by Xia et al. [45] in a hot deformed Mg–Zn–Y–Zr alloy.

Further characterization of the second phase particles for the different experimental conditions was carried out using the FESEM and the results are reported in Fig. 6. FESEM micrographs and EDS results reveal two types of second phase particles: (I) the large particles with a size of 1–5 μm rich in Zn and Ca ($Mg_6Zn_3Ca_2$) and (II) fine spherical particles with a size of 10–100 nm enriched with Mn expected to be α-Mn [46]. The EDS elemental map as shown in Fig. 6 indicates that the Mn element distribution is more uniform in comparison with Zn and Ca elements in homogenized alloy while small concentration of points indicating relatively large Mn particles is observed in the microstructure.

After HECAP treatment, the α-Mn precipitates (fine spherical particles) was clearly observed associated with $Mg_6Zn_3Ca_2$ precipitates (Fig. 6(d and e)). Jiang et al. [47] also observed the presence of 5–20 nm spherical particles rich in Mn during hot extrusion of Mg–Zn–Ca–Mn alloy. Others confirmed these findings and further reported that the fine spherical particles are α-Mn which are uniformly distributed in the extruded microstructure and restrict the grain growth by Zener drag (Zener pinning) [48,49]. Celikin et al. [50] reported that α-Mn phase can dynamically precipitate on the dislocations generated during the deformation process which acts as heterogeneous nucleation sites.
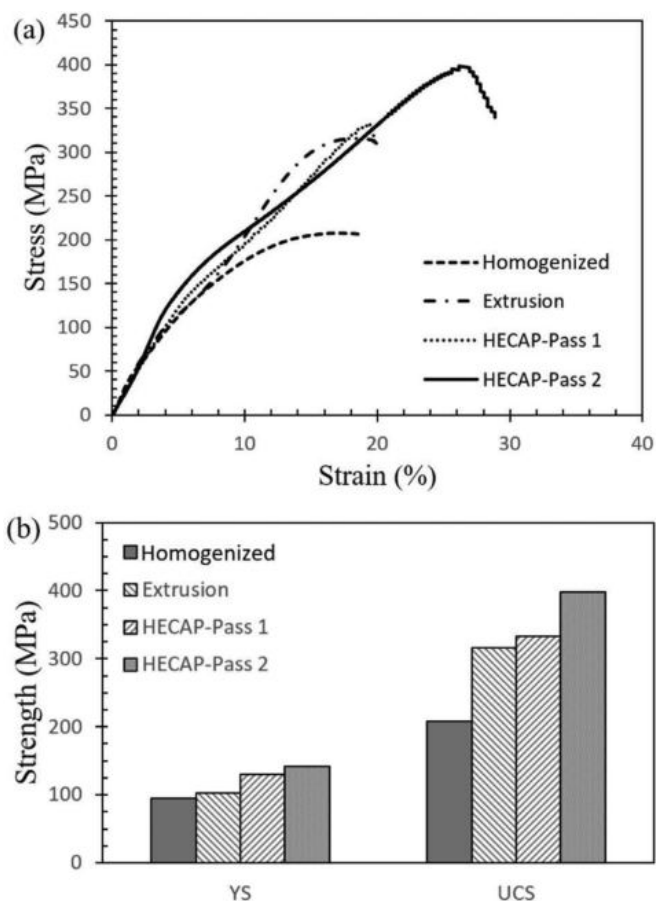

Fig. 7. Compressive mechanical properties of Mg–Zn–Ca–Mn alloy at room temperature; (a) stress-strain curve, (b) mechanical strength.

3.2. Mechanical properties

The stress–strain curves of homogenized, extruded and HECAPed Mg–Zn–Ca–Mn samples after uniaxial

Table 3
Mechanical characteristics of the investigated Mg–Zn–Ca–Mn alloy at different conditions.

Sample	Compression properties			Tensile properties		
	YS (MPa)	UCS (MPa)	Failure strain (%)	YS (MPa)	UTS (MPa)	Failure strain (%)
Homogenized	95	208	19.30	60	140	11.51
Extrusion	103	318	20.09	135	238	14.53
One-pass HECAP	130	332	21.50	145	246	15.82
Two-pass HECAP	142	398.	31.05	185	342	23.22

compression test are reported in Fig. 7. All curves exhibit work hardening until the peak stress followed by a stress drop with further strain due to fracture (Fig. 7(a)). Generally, in the elastic region, or at the start of deformation, the stress increases with increasing the strain until reaching the yield stress due to the nucleation and pile-up of dislocations. In the work hardening region, the increment of dislocation density, interaction of dislocations with grain boundaries and precipitation particles lead to dislocations pile-up and prevent dislocations from further movements throughout the microstructure [51]. Then, the stress drops by further increment of strain owing to the crack propagation and subsequently sample fracture.

Generally, the compressive strengths, YCS and UCS, of the Mg alloy increase considerably after two passes of HECAP process with respect to the cast and homogenized conditions from 95.14 MPa to 142.36 MPa and 207.84 MPa to 398.32 MPa, respectively. Also, the compressive failure strain increases considerably from 19.30 to 31 after two passes of HECAP process. This increase can be attributed to uniform and grain refining microstructure and presence of fine precipitates with uniform distribution in the wrought alloy. In addition, a comparison of the area under the stress–strain curves, as an indication of toughness shows that the three deformed samples have higher toughness than the homogenized one. This is an important finding in load-bearing applications which the material must have high toughness levels [52].

The stress–strain curves of the tension tests for all the samples are reported in Fig. 8. The results show that the homogenized alloy has the lowest strength and plasticity and fails early, probably due to its coarse grain structure [53]. As indicated in Fig. 8(b, c) and Table 3, thermomechanical process and SPD treatment have a significant impact on tension properties of the investigated alloy. Both strength and elongation to fracture in extruded and HECAPed samples are improved by two and three times compared to the homogenized alloy, respectively. This could be related to the finer and equiaxed grains of the extruded and HECAPed samples. However, the dispersion of $Mg_6Zn_3Ca_2$ precipitations at the grain boundaries and grain interiors causes the increment of strength and decrement of elongation to fracture [53].

It has been reported that the strength of Mg alloys is related to the grain size according to the Hall–Petch law ($\sigma_Y = \sigma_0 + kd^{-1/2}$) where σ_0 and k are constants, d is the grain size. As mentioned before, the average grain size of the homogenized, extruded, one and two-pass HECAPed

samples was 347.26 μm, 16.46 μm, 14.64 μm and 2.24 μm, respectively. These values could be correlated with the strength of the corresponding conditions and further confirm that the grain refinement as well as precipitation along grain boundaries result in impediment of dislocation movement thereby increasing the alloy strength.

It is worth mentioning that the elongation of one-pass HECAPed sample was similar to the extruded sample. As reported in Fig. 3(b, e), the grain sizes are very close for the two samples. However, the HECAPed sample exhibits a more inhomogeneous microstructure than extruded sample, probably due to the large amount of non-uniform strains induced by HECAP. It has been reported that such inhomogeneous microstructure, which consists of large grains alongside small ones, is detrimental for elongation [54,55].

The fracture surface of tensile samples of the investigated Mg–Zn–Ca–Mn alloy under different conditions are illustrated in Fig. 9. As seen in Fig. 9(a), the homogenized sample shows cleavage facets and steps (brittle fracture) as well as dimples whereas for the extruded and HECAPed samples a large number of dimples with various sizes can be seen, confirming a ductile fracture mode [56,57]. The higher number of dimples represents the higher ductility of the material, as can be seen in Fig. 9(b–d). The results reveal a transition from brittle fracture (cleavage fracture) of the homogenized samples to ductile fracture mode for the extruded and HECAPed samples as a result of deformation. As reported by Fu et al. [58], during deformation processing, the activation of non-basal slip dislocations as well as grain boundary sliding changes the fracture pattern from brittle to ductile.

3.3. Bio-Corrosion characteristic

3.3.1. Electrochemical behavior

The potentiodynamic polarization diagram of the four examined conditions is shown in Fig. 10. The Tafel extrapolation method in PDP curves was used to obtain the electrochemical parameters such as corrosion current density (i_{corr}), corrosion potential (E_{corr}) and corrosion rate, as listed in Table 4. In the case of PDP diagram of Mg alloys, hydrogen evolution is the dominant mechanism for more negative potentials than E_{corr} whereas the dissolution of Mg is the one at more positive potentials in comparison with E_{corr}, as suggested by Shi et al. [59]. All samples exhibit passivation-like region in anodic polarization curves. As can be seen in Fig. 10(a), thermomechanical process and SPD cause shifting the corrosion potential towards more noble potential and
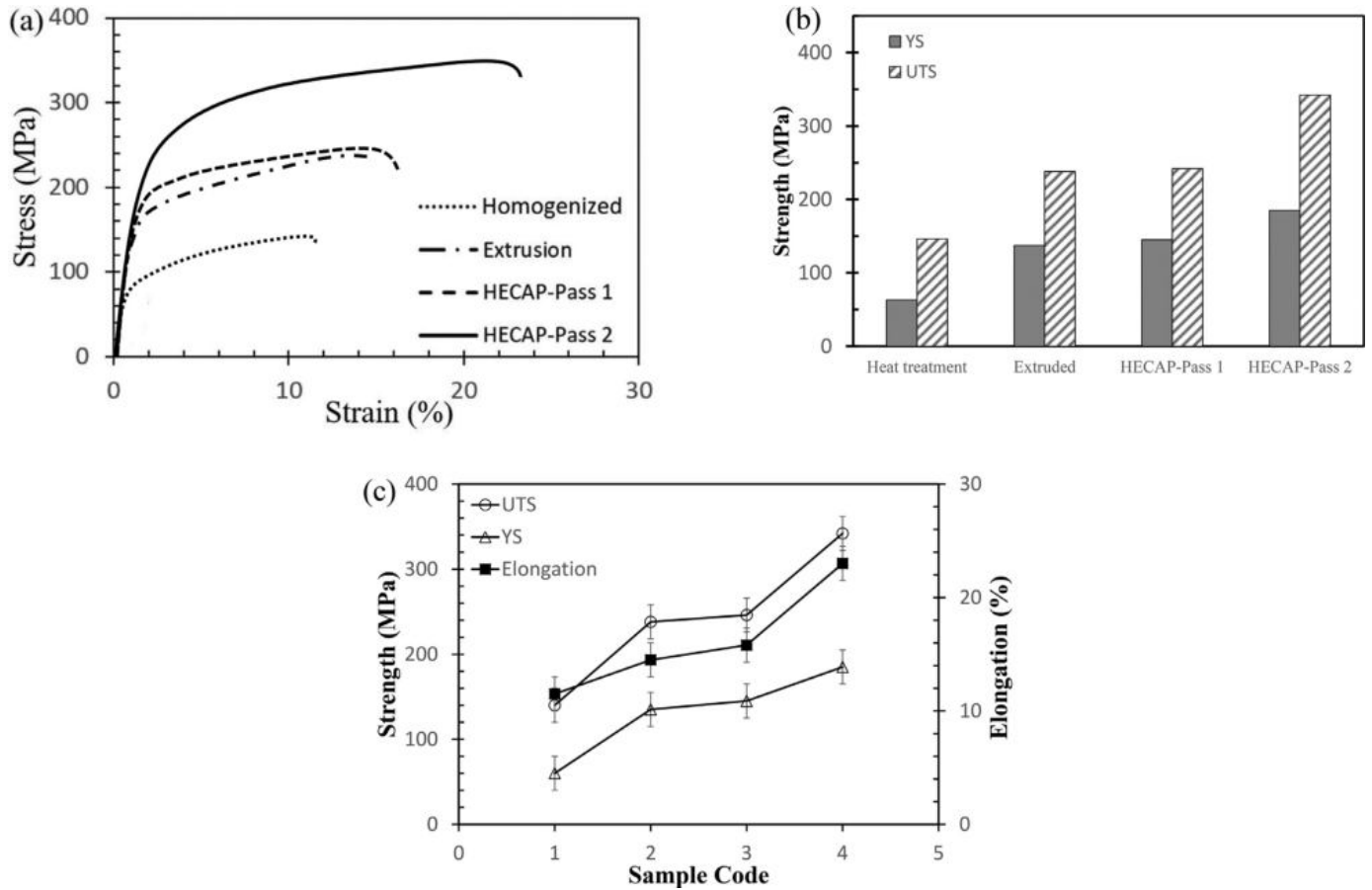
Fig. 8. Tensile mechanical properties of Mg–Zn–Ca–Mn alloy at room temperature; (a) stress-strain curve, (b) mechanical strength (c) mechanical characteristics (1, 2, 3 and 4 refer to the heat treated, extruded, one-pass HECAPed and two-pass HECAPed samples, respectively).

Table 4
Corrosion parameters of Mg–Zn–Ca–Mn alloy at different conditions.

Sample	E_{corr} (V)	i_{corr} (A/cm^2)	Corrosion rate, P_i (mm/y)
Homogenized	−1.66	6.59×10^{-6}	0.142
Extrusion	−1.55	4.36×10^{-6}	0.087
One-pass HECAP	−1.52	3.41×10^{-6}	0.074
Two-pass HECAP	−1.49	2.57×10^{-6}	0.058

reduction of corrosion current density, which subsequently increase the corrosion resistance or decrease the corrosion rate. The test results clearly reveal the lowest corrosion potential and highest corrosion rate for the homogenized sample compared to the extruded and HECAPed ones.

The corrosion current density of the two-pass HECAPed sample is nearly one-third that of the homogenized one and has the lowest corrosion current density among all samples (Table 4). This can be related to the formation of the loose corrosion layer on the surface of the homogenized which cannot effectively protect the alloy from further corrosion. Also, the formation of galvanic couple between the α-Mg matrix and $Mg_6Zn_3Ca_2$ particles can accelerate the dissolution rate of the homogenized sample. However, in the extruded and HECAPed samples, the formation of the hydroxyapatite (HA) protective layer on the surface of the Mg–Zn–Ca–Mn alloy

leads to a remarkable enhancement of the corrosion resistance. It was suggested that HA layer acts as a barrier for penetration of species such as water or ions rich in Cl$^-$ thereby reducing the corrosion rate of Mg alloys [60,61]. It must be also noted that the structure and morphology of the protective layer can be different for each material condition. For instance, for the homogenized and even extruded samples as exposed to the SBF solution, the presence of some voids and micro-cracks leads to insufficient protection of the sample surface which results in ion transfer from the substrate, as also reported by Fathi et al. [60].

The results reported in Table 4 show that the corrosion potential of thermomechanical and SPD samples shifts to nobler potential indicating that thermomechanical and SPD processes improve the corrosion resistance. Thus, the corrosion resistance of Mg–Zn–Ca–Mn alloy at different conditions based on PDP curves can be classified with the following order: two-pass HECAP > one-pass HECAP > Extrusion > homogenization.

Moreover, the corrosion rate (P_i) can be calculated as follow [62]:

$$P_i = 22.85 i_{corr} \qquad (2)$$

From a corrosion resistance perspective, the microstructure and grain size of Mg alloys exposed to a physiologi-
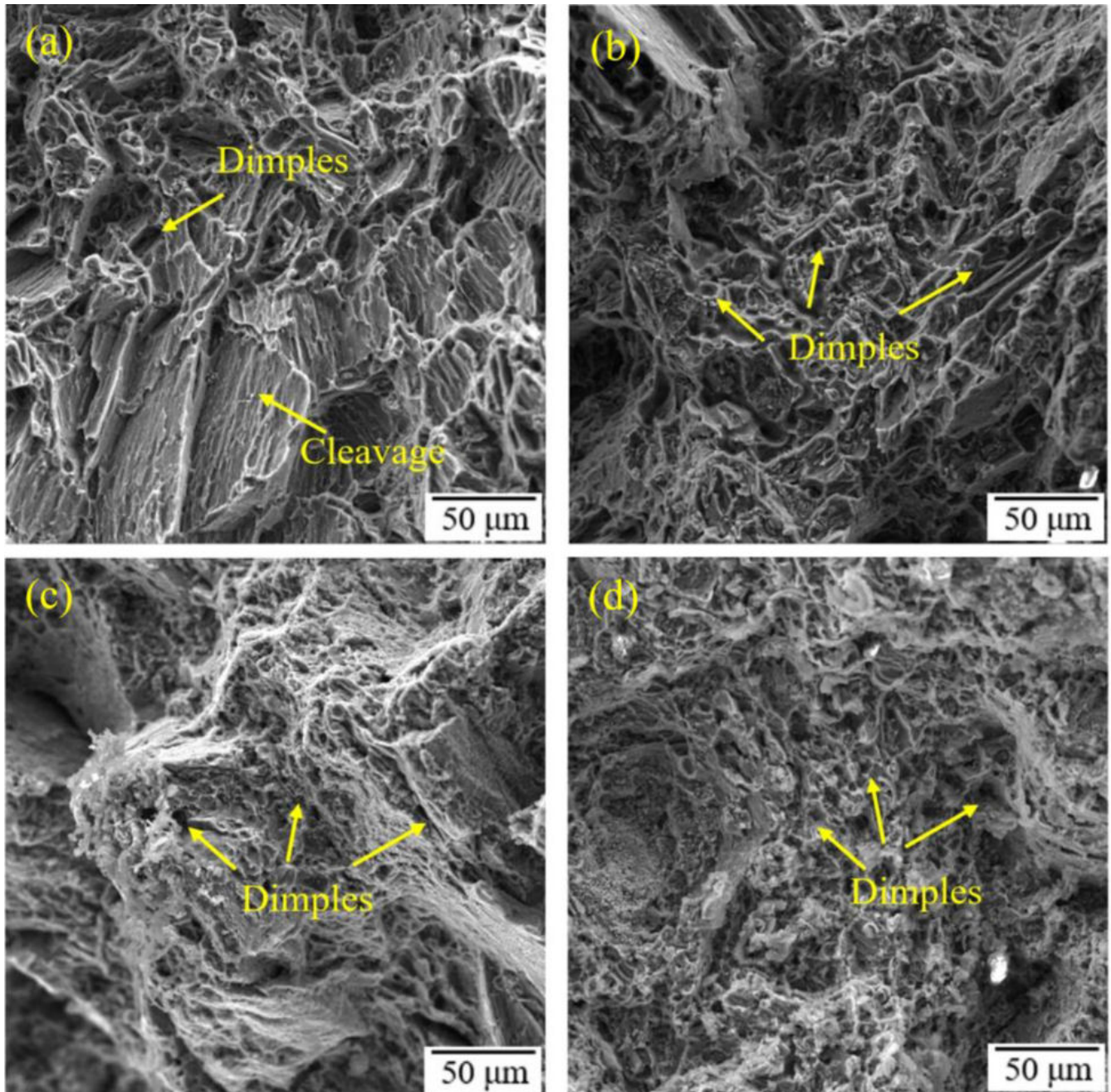
Fig. 9. Fracture morphology of Mg–Zn–Ca–Mn alloy at different conditions of (a) homogenization, (b) extrusion, (c) one-pass HECAP, (d) two-pass HECAP.

cal environment are crucial elements in controlling the extent and severity of the corrosion [63–65]. The increment of grain boundaries leads to decrease in the mismatch between the Mg surface and film layer so that a higher number of grain boundaries bring about more tenacious and adherent protective film layer [37]. Aung and Zhou [63] found that increase in grain size, i.e., reducing the grain boundary length, by heat treatment of AZ31B-H24 alloy leads to an increase in the corrosion rate. Alvarez-Lopez et al. [66] reached a similar conclusion by producing the fine grain microstructure, in a AZ31 alloy processed by ECAP and found that the fine grain Mg alloy has better corrosion resistance than the coarse

grain one. Accordingly, the finer grain size results the more grain boundaries area and consequently the lower corrosion rate will be, as reported by Zhou et al. [67] and Zeng et al. [68].

Moreover, the second phase particles can also play a crucial role on corrosion behavior of magnesium alloys. Generally, the self-corrosion potential of precipitation particles is higher than that of the Mg matrix. Hence, when the magnesium alloy is immersed in the SBF solution, a galvanic corrosion takes place between the particles and Mg matrix. As a result, the matrix near the second phase particles is rapidly corroded. However, if the volume fraction of parti-
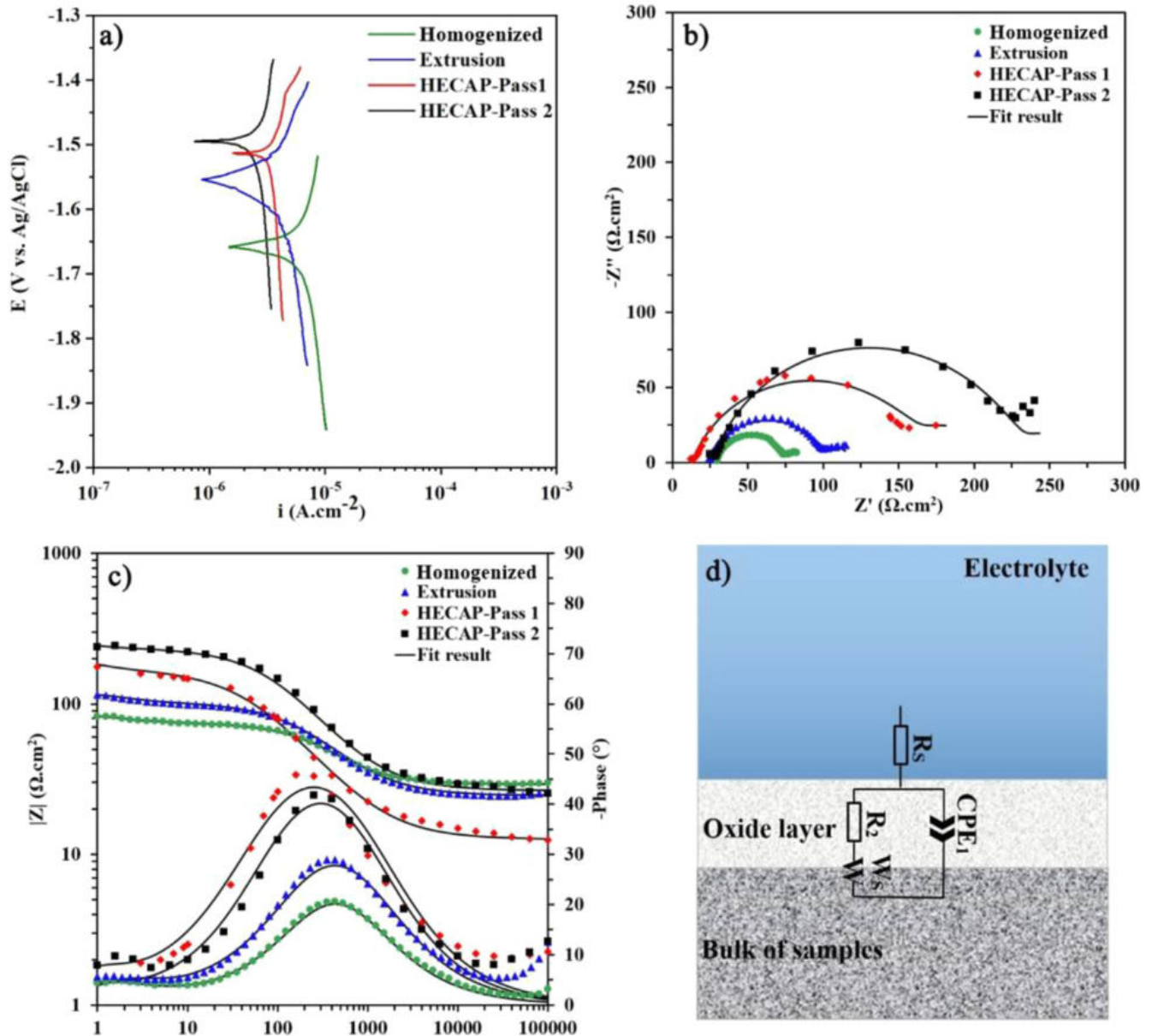
Fig. 10. Electrochemical behavior of Mg–Zn–Ca–Mn alloy in SBF solution; (a) potentiodynamic polarization curve, (b) Nyquist plots, (c) Bode plots and (d) equivalent circuit.

cles is high and precipitation distribution is uniform, a denser and more compact corrosion film layer can be formed on the magnesium substrate. Laleh and Kargar [69] and Zhang et al. [39] who observed that the presence of second phase particles transforms the localized corrosion into a uniform corrosion after mechanical treatment. It must be noted that, if the volume fraction of second phases is low and their distribution is non-uniform, the corrosion film layer is loose and the corrosion rate is actually accelerated.

As mentioned above, it is suggested that since the HECAPed alloy possesses finer grain microstructure, a larger region of the sample can be covered by the protective passive layer. It can be seen in Fig. 10 that the breakdown potential shifts toward more positive values after extrusion and HECAP processes. This behavior demonstrates that higher resistance

to the breakdown of the protective passive film and therefore delay in the onset of pitting corrosion [39].

In order to further investigate the contribution of various parameters on corrosion resistance in the SBF solution, additional EIS measurements were performed. The EIS results of all samples in the SBF solution are plotted in Fig. 10(b,c) with the Nyquist and Bode (impedance module and phase angle shift) representations. The Bode magnitude and phase angle plots for all samples depict the existence of two-time constants. To perform a quantitative comparison between the effect of different interfacial layer constituents (i.e. surface structure and oxide layer), the EIS data were fitted using the equivalent circuit model. The equivalent circuit model was used to fit the EIS results. The corresponding fitting parameters are provided in Table 5.

Table 5
EIS parameters of Mg–Zn–Ca–Mn alloy at different conditions.

Sample	R_S	Q	n	R_2	R_{Ws}	T_{Ws}	C
Homogenization	29.30	4.44×10^{-5}	0.84	45	18.26	0.52	1.39×10^{-5}
Extrusion	24.56	4.68×10^{-5}	0.80	75	28.69	0.45	1.15×10^{-5}
One-pass HECAP	12.6	7.63×10^{-5}	0.77	150	42.01	0.68	2.13×10^{-5}
Two-pass HECAP	26.41	3.22×10^{-5}	0.81	205	31.1	0.76	9.80×10^{-6}

The observed behavior in Fig. 10(b, c) is related to the formation of oxide layer on the surface of sample [39]. As mentioned, the EIS spectra were fitted by an equivalent circuit consisting four elements as schematically presented in Fig. 10(d). In this circuit, RS represents the solute resistance, CPE_1 and R_2 represent the oxide layer and WS represents the electrolyte penetration into the bulk of the samples [39]. The impedance representation of CPE is given by Eq. (3), where Q_c and n are constants, $j^2 = -1$; and ω is the angular frequency. In Eq. (3), the $n = 1$ indicates the pure capacitance, $n = 0.5$ denotes an infinite Warburg (diffusion), $n = 0$ implies a pure resistance and $n = -1$ represents a pure inductance behavior [70]. The true capacitance value for a CPE can be calculated through Eq. (4) [71]:

$$CPE = \frac{1}{Q_C(j\omega)^n} \tag{3}$$

$$C = \frac{(Q_C \times R)^{\left(\frac{1}{n}\right)}}{R} \tag{4}$$

In these equations Q is the CPE constant and is expressed in $(\Omega \cdot cm^{-2} S^{-n})$, which nominally equals to the pure capacitance of the system for $n = 1$; $j^2 = -1$, ω is the angular frequency (rad/s). W_s is thus defined as Eq. (5) where R_{Ws} is the short-range Warburg coefficient, $T_{Ws} = d^2/D$ (d is the effective diffusion thickness, and D is the effective diffusion coefficient of the ion species), and n_{Ws} ranges between 0 and 1 [71].

$$Z_{Ws} = \frac{R_{Ws}\tanh((j\omega T_{Ws})^{0.5}Ws)}{(j\omega T_{Ws})^{0.5}Ws} \tag{5}$$

According to Fig. 10(b, c) and the results reported in Table 5, the impedance values for two-pass HECAPed sample is the largest among the all samples in the following order: two-pass HECAP>one-pass HECAP> extrusion> homogenization, respectively which confirm the obtained data of the PDP analysis in Fig. 10(a).

3.3.2. Hydrogen evolution immersion test

The hydrogen evolution results for all samples are reported in Fig. 11. The results indicate the volume of released hydrogen as a function of time when the Mg alloy is exposed to the SBF solution and reacts with the physiological solution. The lowest amount of released hydrogen gas exhibits the highest corrosion resistance or the lowest corrosion rate. As observed in Fig. 11, the two-pass HECAPed sample possesses the minimum volume of released hydrogen gas whereas the maximum volume belongs to the homogenized one as expected from electrochemical measurements.
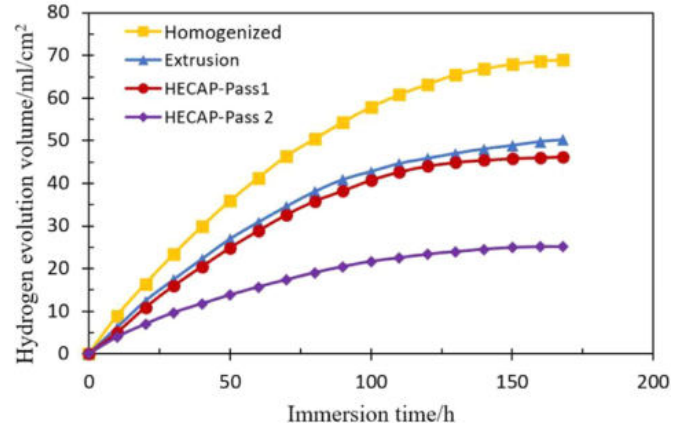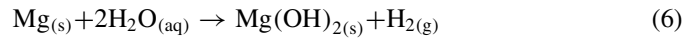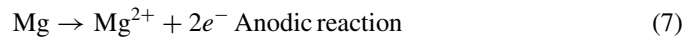

Fig. 11. The hydrogen evolution of Mg–Zn–Ca–Mn alloy as a function of immersion times in SBF at 37 °C at different conditions.

The overall reaction of Mg in corrosion solution and the volume of generated hydrogen can be expressed with the following reaction:

$$Mg_{(s)} + 2H_2O_{(aq)} \rightarrow Mg(OH)_{2(s)} + H_{2(g)} \tag{6}$$

According to the reaction above (Eq. (6)), the dissolution of one mole of Mg generates one mole of hydrogen gas. Hence, theoretically measuring the weight loss of the dissolved Mg is equivalent to the changes in hydrogen evolution due to the degradation of Mg substrate. Thus, the lower is the hydrogen evolution rate, the lower is the corrosion rate and therefore slower degradation rate [72].

Based on Fig. 11, the line slop of hydrogen evolution diagram as a function of time indicates the corrosion rate of the alloy. At the initial immersion times in the SBF solution, the slop increases significantly as time passes, then it grows slowly to reach the steady state. This behavior reveals that the sample is corroded faster during the early immersion hours. The formation of the deposited corrosion layer on the sample surface and dissolution of Mg elements is according to the following reactions:

$$Mg \rightarrow Mg^{2+} + 2e^- \text{ Anodic reaction} \tag{7}$$

$$2H_2O + 2e^- \rightarrow H_2 + 2OH^- \text{ Cathodic reaction} \tag{8}$$

$$Mg^{2+} + 2OH^- \rightarrow Mg(OH)_2 \text{ Overall reaction} \tag{9}$$

Furthermore, Zn can be dissolved and reacts with OH⁻ to form $Zn(OH)_2$:

$$Zn + 2H_2O \rightarrow H_2 + Zn(OH)_2 \tag{10}$$

The Zn hydroxide can precipitate on the sample surface to form protective corrosion film [73]. The solubility of $Zn(OH)_2$ is much less than $Mg(OH)_2$ and can be transformed into the more stable ZnO (Eq. (11)) which improves the corrosion resistance due to its higher protectiveness ability [74].

$$Zn(OH)_2 \rightarrow ZnO + H_2O \tag{11}$$

Based on reaction (7), the dissolution of Mg leads to the transformation of Mg to stable Mg^{2+} as a result of the anodic reaction. On the other hand, the cathodic reaction (reaction (8)) occurs and progresses simultaneously owing to the hydrogen evolution alongside galvanic corrosion. Progress of the anodic reaction brings more dissolution of Mg^{+2} in the SBF as well as more consumption of HCO_3^- and HPO_4^{2-} ions from the SBF solution. This results in increase of Cl^- concentration in the corrosive media. With progressing the reaction, phosphate ions (HPO_4^{2-} and PO_4^{3-}) as well as Ca^{2+} in the SBF solution react with OH^- to form HA on the sample's surface. This reduces the exposed surface area to the SBF solution which subsequently decreases the corrosion rate [40,74,75].

The following sequence of reactions is therefore expected to take place on the sample surface to form the HA:
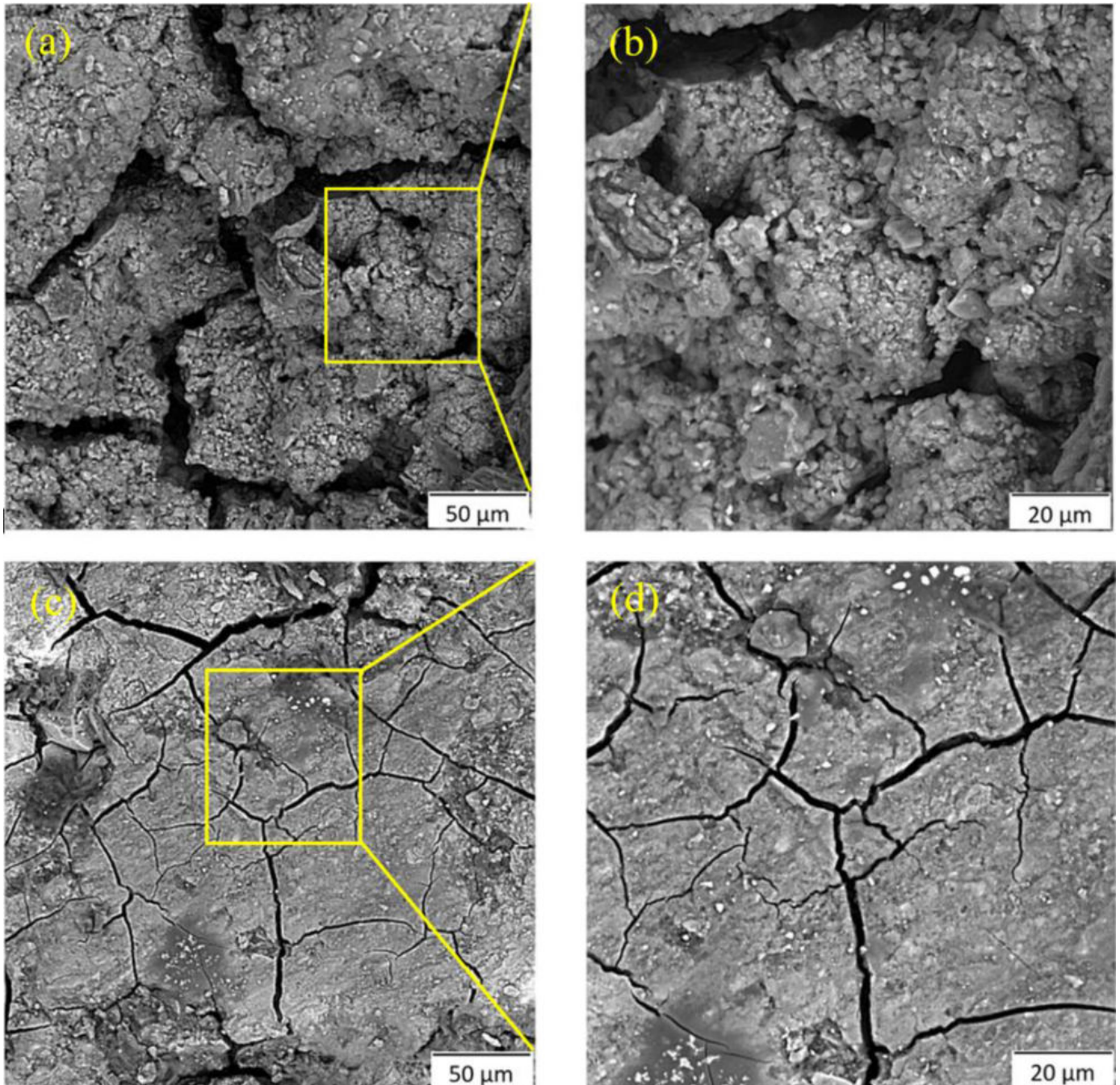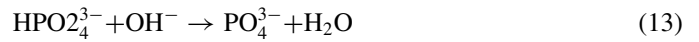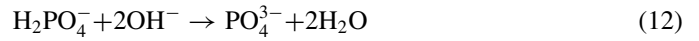
$$H_2PO_4^- + 2OH^- \rightarrow PO_4^{3-} + 2H_2O \qquad (12)$$

$$HPO2_4^{3-} + OH^- \rightarrow PO_4^{3-} + H_2O \qquad (13)$$

Fig. 12. FESEM morphology of Mg–Zn–Ca–Mn alloy after immersion in SFB solution for 7 days: (a, b) homogenization, (c, d) extrusion, (e, f) one-pass HECAP, (g, h) two-pass HECAP, (i) EDS analysis of heat-treated sample, and (j) EDS analysis of two-pass HECAPed sample.
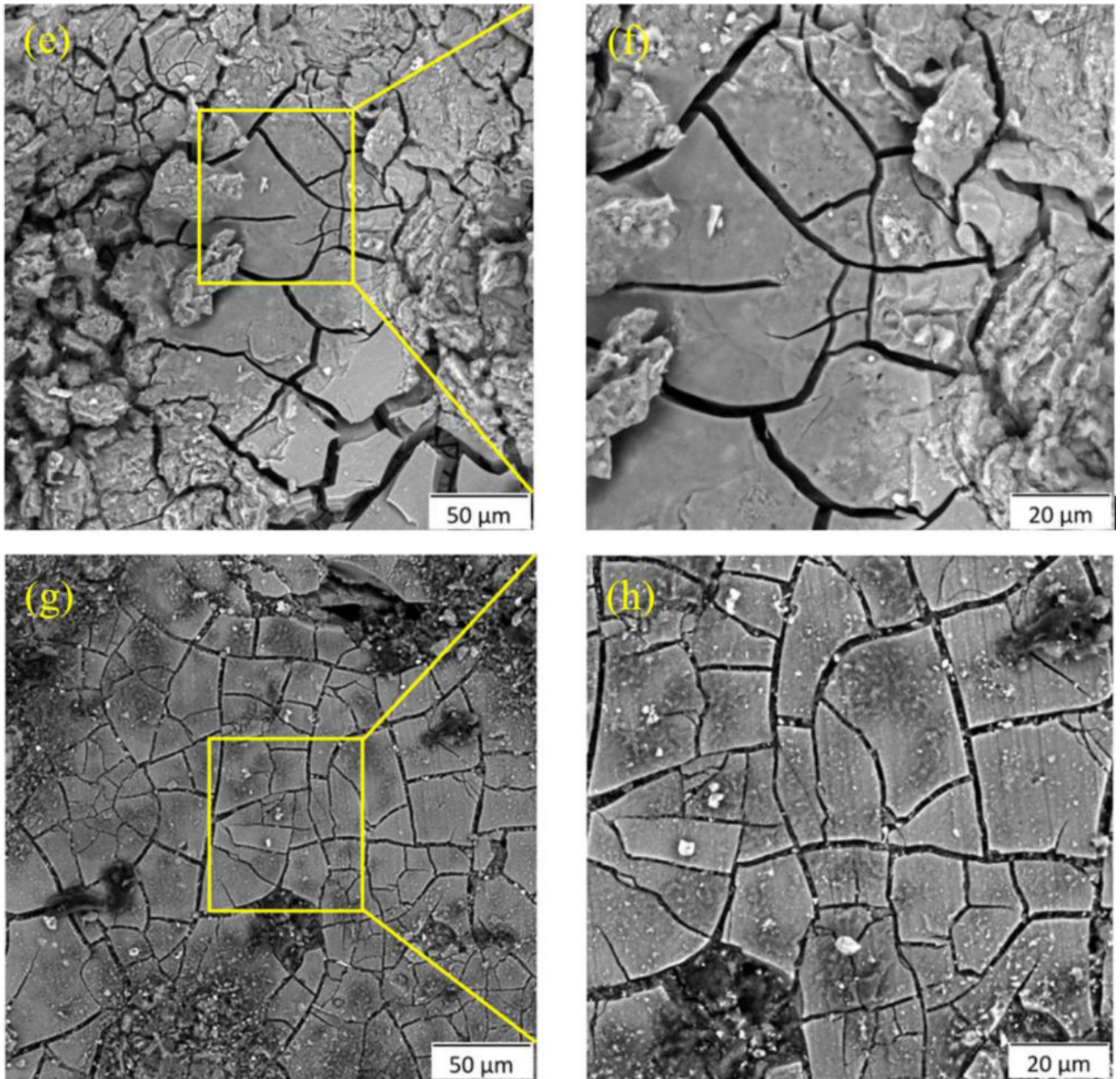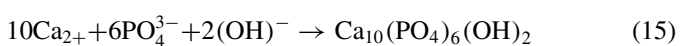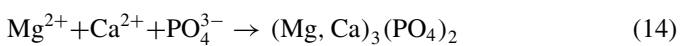
Fig. 12. Continued

$$Mg^{2+}+Ca^{2+}+PO_4^{3-} \rightarrow (Mg, Ca)_3(PO_4)_2 \qquad (14)$$

$$10Ca_{2+}+6PO_4^{3-}+2(OH)^- \rightarrow Ca_{10}(PO_4)_6(OH)_2 \qquad (15)$$

The surface morphology of corroded Mg–Zn–Ca–Mn alloy for the different testing conditions after immersion in the SBF for 7 days in conjunction with EDS results are reported in Fig. 12. As can be seen in Fig. 12(a, b), the entire surface of the homogenized sample is covered by insoluble corrosion film and cracks. The width and thickness of the cracks are different for each sample condition. The largest crack width is found for the homogenized sample and gradually becomes smaller for extruded and then HECAPed samples. The homogenized sample is covered by corrosion products with deep cracks on the sample surface indicating a severe damage of the homogenized sample surface. Also, EDS result (Fig. 12(i)) shows little presence of P and Ca which implies the formation of loose film layer and the destruction of the HA protective layer. However, the presence of O_2 and Mn ions possibly leads to the formation of MnO and MnO_2 which reduces the corrosion rate.

(i)

Element	Wt%	At%
O	87.13	91.41
Mg	8.06	5.55
P	0.22	0.12
Cl	2.58	2.28
Ca	0.35	0.15
Mn	0.88	0.26
Zn	0.78	0.23

(j)

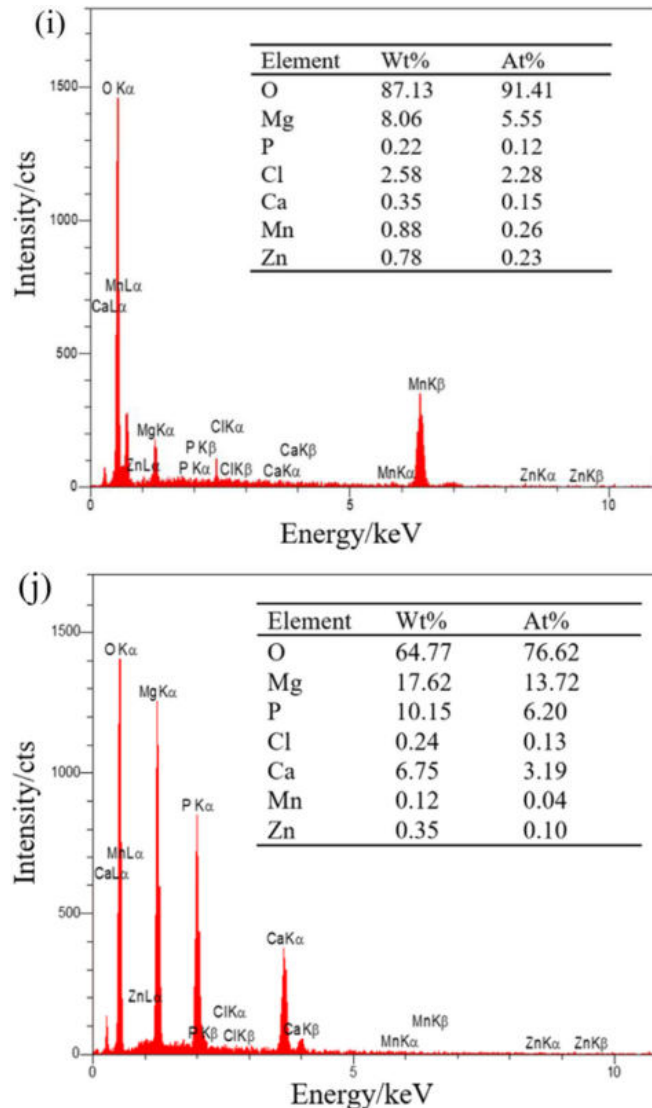| Element	Wt%	At%
O	64.77	76.62
Mg	17.62	13.72
P	10.15	6.20
Cl	0.24	0.13
Ca	6.75	3.19
Mn	0.12	0.04
Zn	0.35	0.10

Fig. 12. Continued

In contrast to homogenized sample, the surface of the wrought alloys exhibits a large number of cracks with different widths. A larger crack thickness implies that the corrosion products layer is loose, whereas a smaller crack thickness is representative of the formation of dense corrosion products, as can be seen in Fig. 12(c–h). The EDS result (Fig. 12(j)) shows that the presence of calcium, phosphorus, oxygen and manganese which indicates the formation of HA as well as MnO and MnO_2. Hence, the higher corrosion resistance or lower degradation rate of the two passes of HECAPed sample can be related to a more stable and adhesive HA protective layer. It has been reported that the existence of phosphate leads to the interruption of chloride ions subsequently slowing down the dissolution of Mg [62]. The formation of HA protective layer on the sample surface can enhance the healing of bone tissue with good biocompatibility. With the increment of immersion time, the passive film layer becomes more compact on the grain boundaries as far as the film growth is restricted due to the limitation of ions diffusion into the film layer [16].

A proposed degradation mechanism for the investigated alloy is schematically shown in Fig. 13 which can be summarized as follows: in the initial hours of immersion of the magnesium alloy in the SBF solution, the entire sample's surface is exposed and Mg atoms are transformed to Mg^{2+} increasing the biodegradation rate. In addition, as a result of cathodic reaction, OH^- and hydrogen are generated thereby, further increasing the corrosion rate. However, with increasing the immersion time, phosphate ions, as well as Ca^{2+} in the SBF solution, react with OH^- to form the HA protective film layer on sample's surface which reduces the total surface area exposed to the SBF solution and results in the overall reduction of the corrosion rate.
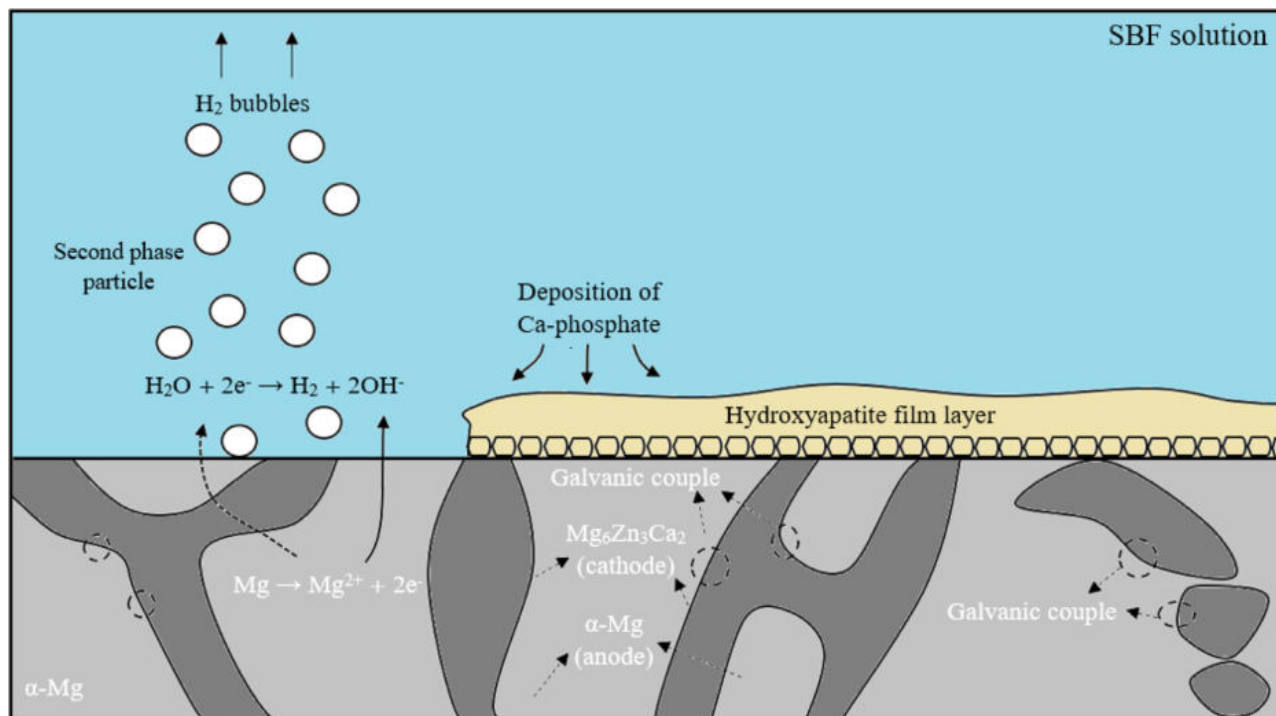
Fig. 13. Schematic representation of degradation mechanism of Mg–Zn–Ca–Mn alloy in SBF solution.

3.4. Texture

The S-shaped compressive curves of extruded and HECAPed samples with remarkable work hardening could be used to identify the deformation mechanism. As can be seen in Fig. 7, in the plastic region of the extruded and HECAPed samples, a drop is observed which is indicative for twinning activity. Twining activity in the compressive deformation is affected by texture. Fig. 14 shows pole figures of extruded, one-pass and two-pass HECAPed samples. As seen, homogenized sample shows randomly texture while the basal texture is domaninat in deformed samples. Maximum pole intensity for extruded and one-pass and two-pass HECAPed samples is 22.82 and 20.97 and 32.56, respectively. More maximum pole intensity and fine grain microstructure in deformed sample after tow passes of HECAP indicate more fraction of grains have been arranged as their c-axis is perpendicular to ED. Typical slip systems in magnesium and its alloys are the basal slip system and prismatic slip systems along $\langle a \rangle$ direction namely, $(0002)\langle 1020 \rangle$ and $\{10\bar{1}0\}\langle 11\bar{2}0 \rangle$, respectively [49]. In order to accommodate strain along $\langle c+a \rangle$ pyramidal slip system of $\{11\bar{2}2\}\langle \bar{1}\bar{1}23 \rangle$ or twinning of $\{10\bar{1}2\}\langle 10\bar{1}1 \rangle$ needs to be activated. Since the pyramidal slip is thermal dependent, then the twin component which is the non-thermal dependent and has a lower critical resolved shear stress (CRSS) can be activated under this situation to satisfy deformation requirement [76,77]. Therefore, at room temperature stronger basal texture in deformed alloys decreases basal slip activity while promotes extraction twinning in compressive test and causes strengthening during the tensile test.

Also, twins can affect elongation during tensile test. Fracture of magnesium alloys mostly initiates at twins. The results observed in Fig. 3 show that after two passes of HECAP, twin-free grains are produced. This indicates that the formation of twin is prevented by HECAP due to the grain refinement as well as texture change. Whereas the activation of non-basal slip systems alongside the grain boundary sliding improve due to grain refinement, as reported by Somekawa et al. [78] and Koike et al. [79].

In most of the published studies, it has been reported that surface energy is a significant factor for corrosion resistance of alloys. In other words, the corrosion rate of metallic materials can be determined by atomic density of planes and surface energy [80–84]. The activation energy for the dissolution of a close pack surface is much higher than that of a loose pack surface because a close-packed plane has higher bonding energy due to the higher atomic coordination number [85]. In a hcp structure, the (0002) basal plane has higher surface atomic density than non-basal planes such as $(10\bar{1}0)$ or $(11\bar{2}0)$. Therefore, the atoms in the planes with lower surface energy, such as (0002) dissolve slower than those of higher surface energy [58]. For instance, the dissolution rate of $(10\bar{1}0)$ prismatic and $(11\bar{2}0)$ pyramid planes is about 18–20 times higher than that of the basal plane [80,86].

As mentioned in Fig. 14 where it can be seen that the highest pole density belongs to the basal plane. This indicates that the basal plane of most of the grains is oriented parallel to the extruded direction (or loading direction in the case of HECAPed sample). The basal pole density of the two-pass HECAPed sample is higher than that of all the ones which
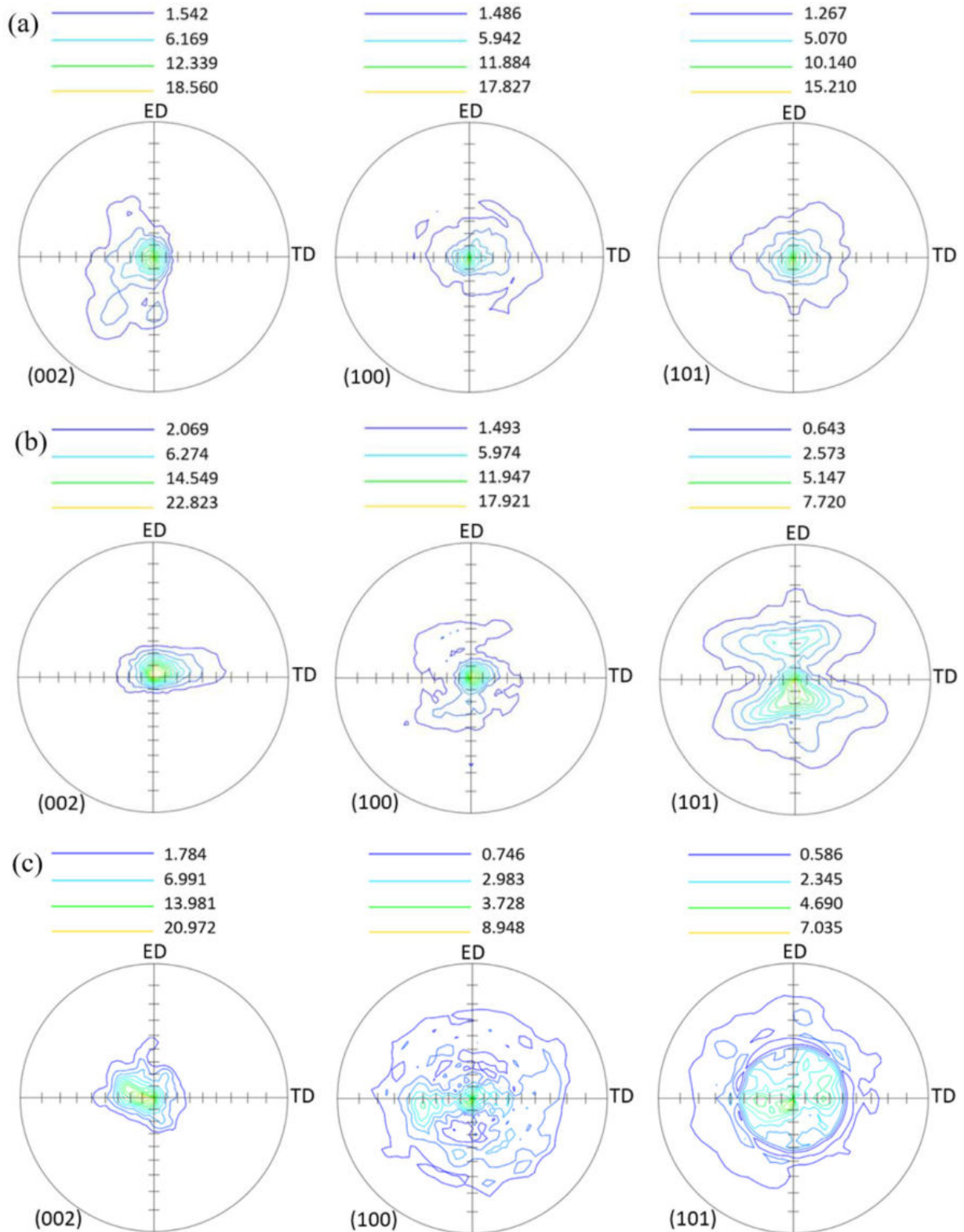
Fig. 14. Pole figures of Mg–Zn–Ca–Mn alloy at different conditions; (a) homogenization, (b) extrusion, (c) one-pass HECAP, (d) two-pass HECAP.

indicates a large number of the grain orientations tends to reorient along (0002). Such increase in the number of (0002) oriented grains is beneficial to the enhancement of corrosion resistance, as also reported in [87]. Song et al.

[80] investigated the effect of texture and microstructure on the corrosion resistance of AZ31 magnesium alloy. They found that the samples with high basal pole densities have the lowest weight loss rate than those with a fiber texture.

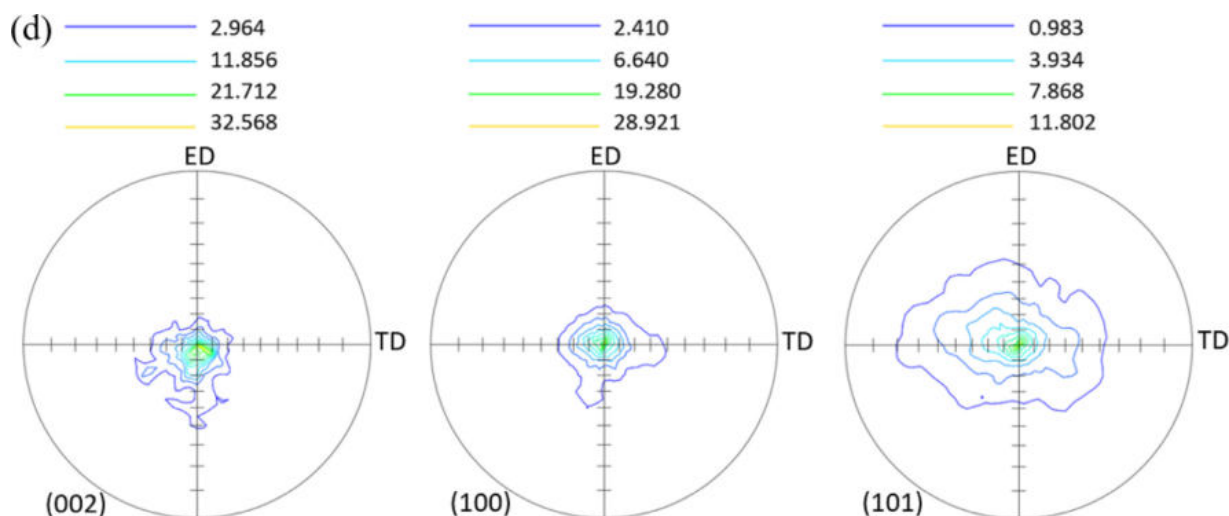| (d)		
2.964	2.410	0.983
11.856	6.640	3.934
21.712	19.280	7.868
32.568	28.921	11.802

(002) (100) (101)

Fig. 14. Continued

Song [85] also reported that the grains with a surface parallel to (0001) basal plane have lower dissolution rate compared to those parallel to $\{01\bar{1}0\}$ prismatic plane. The lower dissolution rate of the basal plane can be correlated to the higher atomic coordination and in turn to higher binding energy which results in lower dissolution rate of atomic close-packed planes. Xin et al. [88] considered the effect of texture on corrosion rate of AZ31 alloy. They concluded that the surface of the grains nearly parallel to (0001) basal plane or the grains near (0001) orientation have the highest corrosion resistance whereas those with $(10\bar{1}0)$ and $(11\bar{2}0)$ orientations have the lowest corrosion resistance. Therefore, higher atomic packing density of some crystallographic planes is associated with higher atomic coordination, higher binding energy and lower surface energy. This results in higher activation energy for dissolution of atoms and eventually higher corrosion resistance.

4. Conclusion

In the present study, the microstructure, mechanical properties at room temperature and bio-corrosion performance in SBF at 37 °C of a Mg–Zn–Ca–Mn alloy under different conditions, were investigated. The following conclusions can be drawn from the present study:

(1) The grain size of Mg–Zn–Ca–Mn alloy was remarkably refined after extrusion and HECAP particularly after a two-pass process because of the occurrence of dynamic recrystallization. The grain size distribution of extruded alloy was inhomogeneous whereas that of the two-pass HECAPed sample was homogeneous with an average grain size of about $2\,\mu m$.

(2) The volume fraction of second phase particles ($Mg_6Zn_3Ca_2$) reduced after two passes of HECAP as uniformly distributed throughout the microstructure compared to the homogenized and extruded ones. This could be ascribed to the presence of diffusion paths for the dissolution of precipitates as well as fragmentation of second phase particles due to the high pressure induced by the HECAP treatment.

(3) The mechanical properties of investigated alloy were significantly improved after two passes of HECAP. The compressive strength and tensile strength after two passes of HECAP were about 398 MPa and 342 MPa, respectively due to the grain refinement and precipitation strengthening. Furthermore, the elongation of this alloy was over 20% possibly related to the homogeneous and uniform grain size distribution.

(4) The electrochemical results showed that the two-pass HECAPed sample has the highest corrosion resistance, followed by the one-pass HECAPed, extruded and homogenized conditions. The lowest corrosion rate of two-pass HECAPed sample could be correlated with its uniform grain refined microstructure which allows the deposition of a more tenacious protective film layer on the grain boundaries.

(5) Immersion tests revealed that the degradation rate of all samples decreases with increase in the immersion time. However, the lowest degradation rate was corresponded to the two-pass HECAPed sample. The uniform fine grain microstructure of this sample and the formation of a more compact and denser protective layer on the substrate as well as the smallest crack width likely resulted in better bio-corrosion resistance.

(6) Based on pole figure results, the two-pass HECAPed sample has the highest basal plane pole density which have the lowest surface energy for the dissolution of atoms and shows the highest corrosion resistance compared to other tested conditions.

Declaration of Competing Interest

None of the authors has any conflict of interest to declare.

References

[1] L. Yang, E. Zhang, Mater. Sci. Eng. C 29 (5) (2009) 1691–1696.

[2] Y.F. Zheng, X.N. Gu, Y.L. Xi, D.L. Chai, Acta Biomater. 6 (5) (2010) 1783–1791.

[3] S. Ramezanzade, G.R. Ebrahimi, M. Torabi Parizi, H.R. Ezatpour, Mater. Sci. Eng. A. 761 (2019) 138025.

[4] B.S. Padekar, R.K. Singh Raman, V.S. Raja, L. Paul, Corros. Sci. 71 (2013) 1–9.

[5] S. Ramezanzade, G.R. Ebrahimi, M. Torabi Parizi, H.R. Ezatpour, J. Compos. Mater. 54 (5) (2020) 711–728.

[6] G. Jin, H. Cao, Y. Qiao, F. Meng, H. Zhu, X. Liu, Colloids Surf. B. Biointerfaces 117 (2014) 158–165.

[7] H. Zreiqat, C.R. Howlett, A. Zannettino, P. Evans, G. Schulze-Tanzil, C. Knabe, M. Shakibaei, J. Biomed. Mater. Res. 62 (2) (2002) 175–184.

[8] S. Miao, K. Cheng, W. Weng, P. Du, G. Shen, G. Han, W. Yan, S. Zhang, Acta Biomater. 4 (2) (2008) 441–446.

[9] D.H. Cho, B.W. Lee, J.Y. Park, K.M. Cho, I.M. Park, J. Alloys Compd. 695 (2017) 1166–1174.

[10] Z. Li, X. Gu, S. Lou, Y. Zheng, Biomaterials 29 (10) (2008) 1329–1344.

[11] S. Zhang, X. Zhang, C. Zhao, J. Li, Y. Song, C. Xie, H. Tao, Y. Zhang, Y. He, Y. Jiang, Y. Bian, Acta Biomater. 6 (2) (2010) 626–640.

[12] B. Zhang, Y. Hou, X. Wang, Y. Wang, L. Geng, Mater. Sci. Eng. C 31 (8) (2011) 1667–1673.

[13] E. Zhang, L. Yang, Mater. Sci. Eng. A 497 (1) (2008) 111–118.

[14] Y.S. Jeong, W.J. Kim, Corros. Sci. 82 (2014) 392–403.

[15] X.N. Gu, N. Li, Y.F. Zheng, L. Ruan, Mater. Sci. Eng. B 176 (20) (2011) 1778–1784.

[16] X. Zhang, G. Yuan, L. Mao, J. Niu, P. Fu, W. Ding, J. Mech. Behav. Biomed. Mater. 7 (2012) 77–86.

[17] R.Z. Valiev, R.K. Islamgaliev, I.V. Alexandrov, Prog. Mater. Sci. 45 (2000) 103–189.

[18] P. Minárik, R. Král, J. Pešička, S. Danis, M. Janecek, Mater. Charact. 112 (2016) 1–10.

[19] C.Z. Zhang, S.J. Zhu, L.G. Wang, R.M. Guo, G.C. Yue, S.K. Guan, Mater. Des. 96 (2016) 54–62.

[20] B. Mani, M. Jahedi, M.H. Paydar, Mater. Sci. Eng. A 528 (2011) 4159–4165.

[21] O. Bouaziz, Y. Estrin, H.S. Kim, Adv. Eng. Mater. 11 (2009) 982–985.

[22] Y. Beygelzimer, V. Varyukhin, S. Synkov, Int. J. Mater. Form. 1 (2008) 443–446.

[23] Y. Beygelzimer, D. Prilepo, R. Kulagin, V. Grishaev, O. Abramova, V. Varyukhin, M. Kulakov, J. Mater. Proc. Technol. 211 (2011) 522–529.

[24] N. Pardis, R. Ebrahimi, Mater. Sci. Eng. A 527 (2009) 355–360.

[25] M. Shamsborhan, A. Shokuhfar, Proc. Inst. Mech. Eng. Part C: J. Mech. Eng. Sci. 228 (2014) 2246–2250.

[26] A. Zangiabadi, M. Kazeminezhad, Mater. Sci. Eng. A 528 (2011) 5066–5072.

[27] S.J. Zhu, Q. Wu, L.G. Wang, Q. Liu, G.C. Yue, S.K. Guan, Mater. Sci. Forum 745–746 (2013) 28–32.

[28] V.M. Segal, Shear-extrusion method, Google Patents, (2006).

[29] G.R. Ebrahimi, A. Barghamadi, H.R. Ezatpour, A. Amiri, J. Manuf. Proc. 47 (2019) 427–436.

[30] J.H. Gao, S.K. Guan, Z.W. Ren, Y.F. Sun, S.J. Zhu, B. Wang, Mater. Lett. 65 (4) (2011) 691–693.

[31] J.-b. Lin, Q.-d. Wang, Y.-j. Chen, M.-p. Liu, H.J. Roven, Trans. Nonferrous Metals Soc. China 20 (11) (2010) 2081–2085.

[32] Y.J. Chen, Q.D. Wang, H.J. Roven, M. Karlsen, Y.D. Yu, M.P. Liu, J. Hjelen, J. Alloys Compd. 462 (1) (2008) 192–200.

[33] C. op't Hoog, N. Birbilis, Y. Estrin, Adv. Eng. Mater. 10 (6) (2008) 579–582.

[34] C. Zhang, S. Guan, L. Wang, S. Zhu, L. Chang, J. Mater. Res. 32 (6) (2017) 1061–1072.

[35] T. Peng, Q. Wang, J. Lin, M. Liu, H.J. Roven, Mater. Sci. Eng. A 528 (3) (2011) 1143–1148.

[36] Q. Wu, S. Zhu, L. Wang, Q. Liu, G. Yue, J. Wang, S. Guan, J. Mech. Behav. Biomed. Mater. 8 (2012) 1–7.

[37] N. Birbilis, K.D. Ralston, S. Virtanen, H.L. Fraser, C.H.J. Davies, Corros. Sci. 45 (3) (2010) 224–230.

[38] F. Zhang, A. Ma, D. Song, J. Jiang, F. Lu, L. Zhang, D. Yang, J. Chen, J. Rare Earth 33 (1) (2015) 93–101.

[39] Y. Zhang, J. Li, J. Li, J. Alloys Compd. 728 (2017) 37–46.

[40] H. Bakhsheshi-Rad, M. Idris, M. Abdul-Kadir, A. Ourdjini, M. Medraj, M. Daroonparvar, E. Hamzah, Mater. Des. 53 (2014) 283–292.

[41] West Conshohocken, PA 3 (2004).

[42] West Conshohocken, PA (2009).

[43] West Conshohocken, PA (2004).

[44] X. Xia, Q. Chen, S. Huang, J. Lin, C. Hu, Z. Zhao, J. Alloys Compd. 644 (2015) 308–316.

[45] S. Xu, K. Oh-Ishi, H. Sunohara, S. Kamado, Mater. Sci. Eng. A 558 (2012) 356–365.

[46] L.B. Tong, M.Y. Zheng, S.W. Xu, S. Kamado, Y.Z. Du, X.S. Hu, K. Wu, W.M. Gan, H.G. Brokmeier, G.J. Wang, X.Y. Lv, Mater. Sci. Eng. A 528 (2011) 3741–3747.

[47] M. Jiang, C. Xu, T. Nakata, H. Yan, R. Chen, S. Kamado, Mater. Sci. Eng. A 678 (2016) 329–338.

[48] J.P. Hadorn, K. Hantzsche, S. Yi, J. Bohlen, D. Letzig, S.R. Agnew, Metall. Mater. Trans. A 43 (4) (2012) 1363–1375.

[49] J. Robson, D. Henry, B. Davis, Mater. Sci. Eng. A 528 (12) (2011) 4239–4247.

[50] M. Celikin, A.A. Kaya, M. Pekguleryuz, Mater. Sci. Eng. A 534 (2012) 129–141.

[51] F. Witte, F. Feyerabend, P. Maier, J. Fischer, M. Störmer, C. Blawert, W. Dietzel, N. Hort, Biomaterials, 28 (13) (2007) 2163–2174.

[52] F. Beer, E. Johnston, Mechanics of Materials, 2nd ed., McGraw-Hill, New York, 1992 Chap. 2.

[53] Y. Yandong, K. Shuzhen, P. Teng, L. Jie, L. Caixia, Mertallograph. Microstr. Anal. 4 (5) (2015) 381–391.

[54] X. Zhang, G. Yuan, J. Niu, P. Fu, W. Ding, J. Mech. Behav. Biomed. Mater. 9 (2012) 153–162.

[55] L.B. Tong, J.H. Chu, W.T. Sun, Z.H. Jiang, D.N. Zou, K.S. Wang, S. Kamado, M.Y. Zheng, J. Alloys Compd. 825 (2020) 153942.

[56] F. Penghuai, P. Liming, J. Haiyan, C. Jianwei, Z. Chunquan Mater. Sci. Eng., A 486 (1–2) (2008) 183–192.

[57] P. Duley, S. Sanyal, T.K. Bandyopadhyay, S. Mandal, Mater. Sci. Eng. A 784 (2020) 139288.

[58] B.-Q. Fu, W. Liu, Z.-L. Li, Adv. Eng. Mater. 255 (23) (2009) 9348–9357.

[59] Z. Shi, M. Liu, A. Atrens, Corros. Sci. 52 (2) (2010) 579–588.

[60] M.H. Fathi, E.M. Zahrani, A. Zomorodian, J. Mater. Lett. 63 (13) (2009) 1195–1198.

[61] H.R. Bakhsheshi-Rad, M.H. Idris, M.R. Abdul-Kadir, Surf. Coat. Technol. 222 (2013) 79–89.

[62] H. Bakhsheshi-Rad, M. Abdul-Kadir, M. Idris, S. Farahany, Corros. Sci. 64 (2012) 184–197.

[63] G.L. Song, A. Atrens, Adv. Eng. Mater. 1 (1) (1999) 11–33.

[64] L. Xu, G. Yu, E. Zhang, F. Pan, K. Yang, J. Biomed. Mater. Res., A 83 (2007) 703–711.

[65] N.N. Aung, W. Zhou, Corros. Sci. 52 (2) (2010) 589–594.

[66] M. Alvarez-Lopez, M.D. Pereda, J.A. del Valle, M. Fernandez-Lorenzo, M.C. Garcia-Alonso, O.A. Ruano, M.L. Escudero, Acta. Biomater. 6 (5) (2010) 1763–1771.

[67] Y.L. Zhou, Y. Li, D.M. Luo, Y. Ding, P. Hodgson, Mater. Sci. Eng. C Mater. Biol. Appl. 49 (2015) 93–100.

[68] R. Zeng, K.U. Kainer, C. Blawert, W. Dietzel, J. Alloys Compd. 509 (13) (2011) 4462–4469.

[69] M. Laleh, F. Kargar, J. Alloys Compd. 509 (37) (2011) 9150–9156.

[70] S. Hashemi, N. Parvin, Z. Valefi, M. Alishahi, Ceram. Int. 45 (17) (2019) 21108–21119.

[71] A. Lasia, Electrochemical impedance spectroscopy and its applications, in: Modern Aspects of Electrochemistry, Springer, Boston, 2002, pp. 143–248.

[72] M.P. Staiger, A.M. Pietak, J. Huadmai, G. Dias, Biomaterials, 27 (9) (2006) 1728–1734.

[73] K. Aramaki, Corros. Sci. 43 (3) (2001) 591–604.

[74] H.-Y. Ha, J.-Y. Kang, J. Yang, C.D. Yim, B.S. You, Corros. Sci. 75 (2013) 426–433.

[75] N. Pulido-González, B. Torres, S. García-Rodríguez, P. Rodrigo, V. Bonache, P. Hidalgo-Manrique, M. Mohedano, J. Rams, J. Alloys Compd. 831 (2020) 154735.

[76] M.R. Barnett, Z. Keshavarz, A.G. Beer, D. Atwell, Acta Biomater. 52 (17) (2004) 5093–5103.

[77] P. Klimanek, A. Pötzsch, Mater. Sci. Eng. A 324 (1) (2002) 145–150.

[78] H. Somekawa, A. Singh, T. Mukai, Philos. Mag. Lett. 86 (3) (2006) 195–204.

[79] J. Koike, T. Kobayashi, T. Mukai, H. Watanabe, M. Suzuki, K. Maruyama, K.J.A.m. Higashi, Acta Mater. 51 (7) (2003) 2055–2065.

[80] G.-L. Song, R. Mishra, Z.J.E.C. Xu, Electrochem. Commun. 12 (8) (2010) 1009–1012.

[81] B. Davepon, J.W. Schultze, U. König, C. Rosenkranz, Surf. Coat. Technol. 169-170 (2003) 85–90.

[82] M. Liu, D. Qiu, M.-C. Zhao, G. Song, A. Atrens, Scr. Mater. 58 (5) (2008) 421–424.

[83] H. Asgari, M.R. Toroghinejad, M.A. Golozar, J. Mater. Process. Technol. 198 (1) (2008) 54–59.

[84] P.R. Seré, J.D. Culcasi, C.I. Elsner, A.R. Di Sarli, Surf. Coat. Technol. 122 (2) (1999) 143–149.

[85] G.-L. Song, JOM, 64 (6) (2012) 671–679.

[86] G.-L. Song, Z. Xu, Corros. Sci. 63 (2012) 100–112.

[87] G.-L. Song, Z. Xu, Corros. Sci. 63 (2012) 100–112.

[88] R. Xin, B. Li, L. Li, Q. Liu, Mater. Des. 32 (8–9) (2011) 4548–4552.